JCI The Journal of Clinical Investigation

Identification of potent biparatopic antibodies targeting FGFR2 fusion driven cholangiocarcinoma

Saireudee Chaturantabut, … , Nabeel Bardeesy, William R. Sellers

J Clin Invest. 2025. https://doi.org/10.1172/JCI182417.

Research In-Press Preview **Oncology**

Graphical abstract

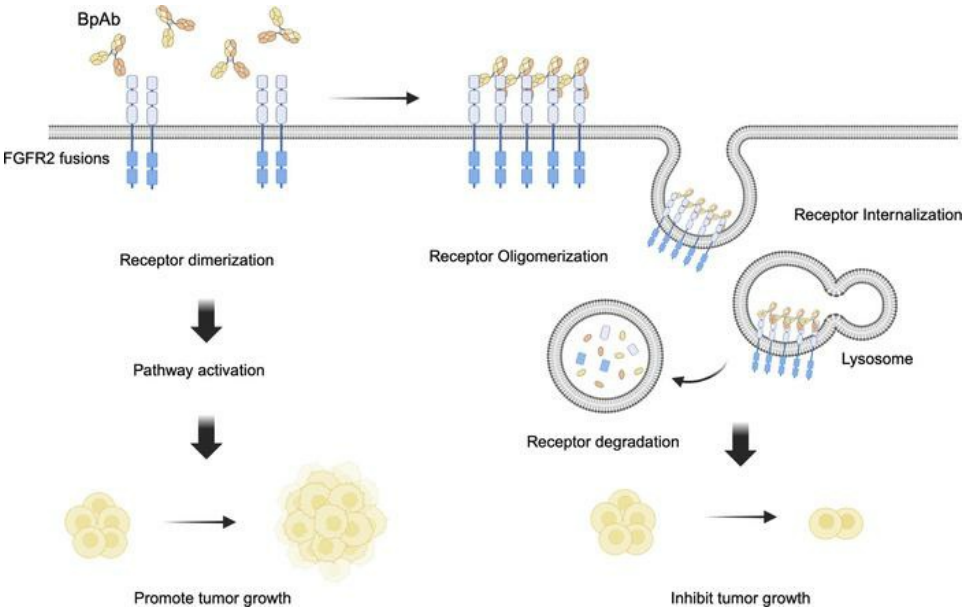

Identification of potent biparatopic antibodies targeting FGFR2 fusion driven cholangiocarcinoma.

Summary:

We identify biparatopic FGFR2 antibodies that are effective against FGFR2 fusion driven cholangiocarcinoma.

Authors:

Saireudee Chaturantabut[1,2,3,4], Sydney Oliver[1], Dennie T. Frederick[1], Jiwan J. Kim[1], Foxy P. Robinson[1], Alessandro Sinopoli[5], Tian-Yu Song[1, 2, 3], Yao He[1], Yuan-Chen Chang[1], Diego J. Rodriguez[1], Liang Chang[1,2,3], Devishi Kesar[1], Meilani Ching[1], Ruvimbo Dzvurumi[1], Adel Atari[1], Yuen-Yi Tseng[1], Nabeel Bardeesy[1,3,5], William R. Sellers[1,2,3*]

Affiliations:

[1]Broad Institute of MIT and Harvard; Cambridge, MA, USA

[2]Dana-Farber Cancer Institute; Boston, MA, USA

[3]Harvard Medical School; Boston, MA, USA

[4] Faculty of Pharmacy, Silpakorn University; Nakhon Pathom 73000, Thailand

[5] Ridgeline Discovery GmbH; Basel, Switzerland

[6] Massachusetts General Hospital Cancer Center; Boston, MA, USA

Correspondence:

Dr. William R. Sellers (W.R.S.)

* Contact Information: Broad Institute of Harvard and MIT

415 Main St. Cambridge, MA 02142, USA

Email: wsellers@broadinstitute.org

Tel: +1 (617)714-7110

Conflict-of-interest:

S.C. received research funding from Ridgeline Discovery. A.S. is an employee of Ridgeline Discovery. L.C. is an employee of Cure Ventures; was an employee of 5AM Ventures and Flagship Pioneering. N. B. has research agreements with Tyra Biosciences, Servier Laboratories, and Kinnate Biopharma. W.R.S. received research fundings from Bayer, Calico, Pfizer, Merck, Ideaya, Novartis Pharmaceuticals, Boehringer-Ingelheim, Ridgeline Discovery, and Bristol-Myers Squibb; and is or was an advisory board member for Epidarex Capital, Ideaya, Pierre Fabre; 2Seventy Bio; and a founder for Red Ridge Bio and Delphia Therapeutics. S.C. and W.R.S. are inventors on US Patent application 63/033,975 covering biparatopic antibodies targeting FGFR2. No potential conflicts of interest were disclosed by the other authors.

Abstract:

Translocations involving FGFR2 gene fusions are common in cholangiocarcinoma and predict response to FGFR kinase inhibitors. However, response rates and durability are limited due to the emergence of resistance, typically involving FGFR2 kinase domain mutations, and to sub-optimal dosing, relating to drug adverse effects. Here, we develop biparatopic antibodies targeting the FGFR2 extracellular domain (ECD), as candidate therapeutics. Biparatopic antibodies can overcome drawbacks of bivalent monospecific antibodies, which often show poor inhibitory or even agonist activity against oncogenic receptors. We show that oncogenic transformation by FGFR2 fusions requires an intact ECD. Moreover, by systematically generating biparatopic antibodies targeting distinct epitope pairs in FGFR2 ECD, we identified antibodies that effectively block signaling and malignant growth driven by FGFR2-fusions. Importantly, these antibodies demonstrate efficacy in vivo, synergy with FGFR inhibitors, and activity against FGFR2 fusions harboring kinase domain mutations. Thus, biparatopic antibodies may serve as an innovative treatment option for patients with FGFR2-altered cholangiocarcinoma.

INTRODUCTION

FGFR2 fusions are found across a variety of cancer types including in 10-15% of primary intrahepatic cholangiocarcinoma (ICC) (1, 2). While three FGFR1-3/4 inhibitors are approved for the treatment of ICC(3), positive trial results are tempered by a short duration of disease control (<9 months) and limited response rates (18-42%)(4). Major challenges of approved FGFR inhibitors include on-target, off-tumor adverse effects and the

emergence of resistance mutations, particularly V565 gatekeeper mutations (3). On-target hyperphosphatemia, attributable to the role of FGFR1 in phosphate homeostasis, limits optimal dosing of FGFR1-3 inhibitors(5). While the recently developed FGFR2 selective kinase inhibitor, RLY-4008, shows increased response rates, its benefits are not durable(6). Consequently, although FGFR2-fusion-positive ICCs exhibit sustained dependence on FGFR2 signaling, targeting the pathway with kinase inhibitors alone is insufficient to achieve the desired therapeutic benefit.

Therapeutic antibodies against the extracellular domain (ECD) of FGFR2 could serve as complementary treatment modalities to FGFR kinase inhibitors, offering the potential for high specificity and retaining efficacy in the setting of kinase domain mutations. Importantly, the ECD is retained in all cases of intracellular fusion events. Thus, the FGFR2 ECD may be amenable to antibody-mediated targeting, although there are key questions and hurdles to address to ensure optimal therapeutic development.

One such question is the uncertainty of whether ligand activation contributes to the transforming capacity of FGFR2 fusions, which has important implications for antibody design. In this regard, antibodies to receptor tyrosine kinases (RTKs) can potentially function by blocking signaling as well as through antibody-dependent cellular cytotoxicity (ADCC) or through cytotoxic payloads(7–9). However, bivalent antibodies against RTKs are often only marginally effective inhibitors of signaling and instead often act through ADCC or antibody-drug conjugate payloads (ADCs) (7–9). Indeed, of currently approved antibodies in cancer, less than 10% exhibit signaling pathway blockade, with over 60%

exerting immune effector functions and over 25% classified as ADCs(10). Furthermore, receptor targeting by some monospecific (monoparatopic) antibodies lead to agonistic activity due to receptor dimerization and activation (11–14). These data suggest that improvements in the activity of traditional monospecific bivalent antibodies could lead to more effective therapeutic antibodies. As a result, distinct antibody formats have been explored.

Here, we developed biparatopic antibodies targeting of FGFR2 fusions in ICC. First, we defined the contributions of the FGFR2 ECD to transformation by FGFR2 fusion alleles. Second, we generated biparatopic antibodies targeting the FGFR2 ECD. Biparatopic antibodies, which recognize two distinct epitopes on the same protein, are a promising format which can produce highly potent antagonists (15–17). By generating all 15 possible combinatorial heterodimeric biparatopic antibodies from 6 optimized monospecific antibodies that bind to distinct epitopes along the FGFR2 ECD, we identified two anti-FGFR2 biparatopic antibodies that are markedly superior to their parental bivalent antibodies in their potency against FGFR2 fusion driven cancers. Our study highlights the potential of biparatopic antibodies targeting FGFR2 as therapeutic agents.

RESULTS

The extracellular domain is necessary for full transformation by FGFR2 fusions.

To ascertain the role of FGFR2-fusion ECDs, we developed BaF3 and NIH3T3 fibroblast cell lines expressing FGFR2 fusions: FGFR2-BICC1 (the most common fusion found in ICC), FGFR2-AHCYL1, and FGFR2-PHGDH proteins. Expression of FGFR2 fusions

resulted in IL-3-independent growth of BaF3 cells and transformation of NIH3T3 cells (Figure 1A and Supplemental Figure 1A); growth of these cells was attenuated by the FGFR inhibitor (FGFRi) infigratinib (Supplemental Figure 1A). Transformation and proliferation of the FGFR2-fusion expressing lines were further enhanced by the FGFR2 ligand, FGF10 (Figure 1A, B). To measure receptor dimerization, we utilized NanoBiT assays that detect protein interactions by proximity-mediated luciferase complementation(18) (Figure 1C). We validated expression of full-length FGFR2-WT and FGFR2-ACHYL1 coupled to the NanoBiT fragments, LgBiT and SmBiT (Supplemental Figure 1B, C) and assayed luminescent activity upon co-expression. Complementation-based luciferase activity of FGFR2 fusions was significantly higher than that of FGFR2-WT (Figure 1D), indicating ligand-independent dimerization. Nonetheless, addition of FGF10 significantly enhanced receptor dimerization of FGFR2-WT and FGFR2-ACHYL1 (Figure 1D). These data indicate that the FGFR2-fusion ECD is functional and enhances fusion receptor activation through ligand-mediated dimerization.

Next, we asked whether subdomains of the ECD were required for FGFR2-fusion dimerization, cell growth and transformation. To this end, we generated FGFR2 fusions with deletions of the D1, D2, and D3 subdomains (Figure 1E). Since the D2 and D3 domains are necessary and sufficient for ligand binding, we also generated D2+3 deletion constructs. Each ECD deletion was expressed in NIH3T3 cells that lack endogenous FGFR2, and we performed colony formation and proliferation assays. Comparable expression of each construct was observed via immunoblotting (Supplemental Figure 1D, E). D1, D2, D3, and D2+3 deletions each reduced growth (35-77% growth inhibition) and

transformation capacity (36-50% reduction) compared to full length (FL) FGFR2-fusion expressing cells (Figure 1F, G, H). Specifically, deletion of D2 of the FGFR2 ECD had a pronounced impact on cell growth and transformation, suggesting that D2 may play a prominent role in the oncogenicity of FGFR2-BICC1. Thus, the ECD is required for full transformation by FGFR2 fusions.

Signaling by FGFR2-WT is initiated by binding of FGF ligands to the D2 and D3 domains leading to receptor dimerization and activation. To test the domain requirement for activity of FGFR2-fusions, we utilized NanoBiT complementation and immunoblotting assays. The D2, D3, and D2+3 deleted FGFR2 fusions showed significantly impaired dimerization in the presence or absence of FGF10 ligand (Figure 1I). In keeping with the autoinhibitory function of the D1 domain(19), loss of the D1 domain enhanced receptor dimerization. Finally, we assessed the downstream pathway activation of the ECD deletion constructs by immunoblotting. Compared to the FL construct, expression of the D2, D3, and D2+3 deletion derivatives showed markedly impaired FGFR2 signaling (reduced p-FGFR (Y653/654), p-FRS2(Y436), and p-ERK(T202/Y204)), whereas the D1 deletion increased FGFR2 signaling output correlating with the observed increase in dimerization (Figure 1I, J, Supplemental Figure 1F). Together, these data demonstrate that the FGFR2-fusion ECD is necessary for full transformation of FGFR2 fusions. We further identify an autoinhibitory function of the D1 domain, deletion of which activates ERK leading to diminished viability, consistent with previous observations of activation dependent lethality we and others observed in BRAF and NRAS mutant setting(20, 21).

Development of candidate biparatopic antibodies directed against FGFR2

To determine whether biparatopic antibodies can disrupt the function of FGFR2 fusions, we identified and produced 6 optimized FGFR2 antibodies(22–25), including the parental antibody of bemarituzumab, an ADCC-enhanced FGFR2 antibody in phase III trials(26). Available data suggested these antibodies likely bind to distinct epitopes in the ECD of FGFR2b, the primary isoform of FGFR2 fusions expressed in ICC(3). We compared and validated the reported binding epitopes and binding affinities, ascertaining FGFR2 binding by flow cytometry and Bio-Layer Interferometry (BLI) Octet analysis. We determined the apparent binding affinities of parental antibodies A-F, finding equilibrium dissociation constants (Kd) ranging from 0.15 nM-32.79 nM (Figure 2A). To validate their binding epitopes, NIH3T3 cells expressing FGFR2-fusion constructs with deletions in D1, D2, D3, or D2+3 (Figure 1E) were analyzed by flow cytometry The data showed that antibody A bound to all constructs, antibody B bound to all except the D1-deleted construct, antibodies C and D bound to all but the D2-deleted construct, and antibodies E and F bound to all except the D3-deleted construct (Figure 2B, Supplemental Figure 2A). These data defined the following binding epitopes: antibody B (D1), antibodies C and D (D2), antibodies E and F (D3), and antibody A (outside the D1-3 domains, likely involving the N-terminus), consistent with prior reports(23). BLI-Octet epitope binning analysis by pairwise cross-competition corroborated our findings, showing antibodies A and B with unique binding epitopes while antibodies C, D and antibodies E, F pairs having overlapping epitopes (Figure 2C, D, Supplemental Figure 2B).

To determine whether targeting FGFR2-fusion ECDs with anti-FGFR2 antibodies impair their oncogenic activity, we treated BaF3 cells expressing FGFR2-PHGDH with each FGFR2 antibody. Antibodies against the ligand-binding domain (antibodies C, D, E, and F) inhibited FGF-stimulated growth (Figure 2E) supporting the notion that FGF ligands augment FGFR2-fusion activity and that the ECD is necessary for FGFR2 fusion driven growth. In the ligand-independent setting, only antibody F inhibited FGFR2-PHGDH driven BaF3 cell growth (Figure 2F). Antibodies B, D, and E had marginal impacts on cell growth in this setting, while antibodies A and C exhibited agonistic activity and promoted ligand-independent growth (Figure 2F). Consistent with its agonist activity, antibody C increased dimerization of FGFR2-ACHYL1 and FGFR2-BICC1 (Supplemental Figure 2C). As is the case with antibodies against the MET receptor that agonize and dimerize the receptors(14), the ligand-independent growth-promoting effects of antibodies A and C may result from unique binding epitopes eliciting antibody-induced dimerization. In addition, the differential activity of antibodies C and D suggests that they bind to distinct epitopes within the D2 domain.

We next asked whether FGFR2 biparatopic antibodies might have enhanced potency and avoid ligand-independent agonism. We used controlled Fab-arm exchange to generate full IgG1 FGFR2 antibodies that simultaneously bind two different epitopes on the FGFR2 ECD(27). Here, complementary IgG Fc mutations force heterodimer formation between distinct IgG-formatted antibodies while maintaining heavy and light chain pairing. We produced each of the 6 parental antibodies with the reciprocal mutations to create 15 unique biparatopics from all pairwise combinations (Figure 3A, B). In mass spectrometry

analysis each biparatopic antibody showed >95% purity with minimal residual parental antibody (as in Supplemental Figure 3A, B). In all, we validated the binding affinities as well as binding epitopes of the 6 parental antibodies and generated 15 biparatopic antibodies for further characterization.

Unbiased screening identifies potent, tumor growth inhibiting biparatopic antibodies

We next assessed antiproliferative activity in FGFR2 fusion driven BaF3 cells with or without addition of ligand. Of the 15 biparatopic antibodies tested, 7 (46%) and 11 (73%) outperformed parental antibodies at inhibiting growth of FGFR2-ACHYL1 driven BaF3 cells in the absence or presence of FGF10 ligand, respectively (Figure 3C, D). A second BaF3 model driven by an FGFR2-PHGDH fusion yielded similar results (Supplemental Figure 3C, D). Notably, bpAb-B/C and bpAb-B/D were the most potent of the 21 parental and biparatopic antibodies in the viability assays. Importantly, the efficacy of pairwise mixtures of the parental antibodies differed from and did not predict the potency of their respective biparatopic antibodies (Supplemental Figure 3E, F), suggesting that distinct modes of action are enabled by the biparatopic format.

We next determined the apparent binding affinity of the biparatopic antibodies for FGFR2. Using the MSD-SET assay, we found that 80% (12 out of 15) of biparatopic antibodies, including bpAb-B/C and bpAb-B/D, had marked improvements (>10 fold) in FGFR2 apparent binding affinities as compared to their parental antibodies (Figure 3E). The remaining 3 biparatopic antibodies with lower affinities had binding epitopes either within

the same ECD subdomain (D2 for bpAb-C/D; D3 for bpAb-E/F) or on subdomains that are the furthest apart (D1 and D3 for bpAb-A/E). These data suggest that the geometry of binding between antibodies and their epitopes plays an important role in achieving high apparent affinity binding. We next determined the binding avidity to FGFR2 expressing cells using acoustic force spectrometry. After binding of antibody-coated beads to FGFR2-PHGDH expressing NIH3T3 cells on the chip, acoustic force ramp from 0 to 1000 pN was applied and antibody detachment from cells was observed using real-time fluorescence imaging. bpAb-B/C and bpAb-B/D had markedly enhanced binding avidity compared to parental antibodies B, C, and D, confirming the affinity data (Figure 3F). Finally, we examined the kinetics of antibody association and dissociation using BLI-Octet analysis. In addition to their enhanced binding avidity, antibodies bpAb-B/C and bpAb-B/D also exhibited slower off-rates and higher apparent affinity (low Kd) compared to their parental antibodies B, C, and D (Supplemental Figure 3G, H). Both bpAb-B/C and bpAb-B/D contain binding arms against epitope B, a flexible autoinhibitory extracellular domain (ECD) D1 (Figure 2D). Together, our data demonstrate that the majority of biparatopic antibodies against combinations of selected epitopes on the FGFR2 ECD have enhanced antitumor activity and cellular binding avidity compared to their parental antibodies. Based on these attributes we selected bpAb-B/C and bpAb-B/D for further characterization.

Biparatopic antibodies show superior inhibition of growth and transformation of FGFR2 fusion driven cholangiocarcinoma cell lines

We investigated the impact of biparatopic FGFR2 antibody candidates bpAb-B/C and bpAb-B/D on two patient-derived models of FGFR2 fusion+ ICC, ICC13-7 (FGFR inhibitor-sensitive) and ICC21 (partially sensitive) (28). ICC13-7 and ICC21 express the endogenous FGFR2-OPTN and FGFR2-CBX5 fusions, respectively. Correlating with their activity in FGFR2 -fusion expressing BaF3 cells, bpAb-B/C and bpAb-B/D have enhanced efficacy at inhibiting growth of ICC13-7 and ICC21 cells in the absence (Figure 4A, C) and, even greater, in the presence (Figure 4B, C) of FGF10 compared to the parental antibodies.

To investigate whether cell growth inhibition caused by bpAb-B/C and bpAb-B/D were specific to inhibition of FGFR2 rather than other FGFRs, extracts from NIH3T3 cells expressing FGFR2-PHGDH were profiled using a phospho-RTK array. We found that bpAb-B/C and bpAb-B/D specifically inhibited phosphorylation of FGFR2 but not of FGFR1 or FGFR3 (Figure 4D, E; minimal FGFR4 phosphorylation was detected in these cells). We also tested FGFR2 specificity using the CCLP-1 ICC cell line, which lacks an FGFR2 fusion and is driven by FGFR1 and FGF20 overexpression(3). Both bpAb-B/C and bpAb-B/D treatments had no significant impact on CCLP-1 cell viability, whereas the IC50 for FGFR1-3 inhibitor futibatinib is <1.5 nM (3) (Figure 4F). Thus, bpAb-B/C and bpAb-B/D inhibit FGFR2 with high specificity.

We next examined the effects of bpAb-B/C and bpAb-B/D on FGFR2-fusion mediated signaling. Both bpAb-B/C and bpAb-B/D robustly decreased p-FGFR, p-FRS2, and p-ERK as compared to their parental antibodies B, C, or D in a ligand-independent setting

(Figure 4G, Supplemental Figure 4A, B, E); additionally, bpAb-B/C and bpAb-B/D blocked FGF10-induced phosphorylation of FGFR, FRS2, and ERK (Figure 4H, Supplemental Figure 4A, B, F). Similarly, bpAb-B/C and bpAb-B/D impaired downstream signaling in NIH3T3 cells expressing FGFR2-PHGDH including p-FGFR, p-FRS2, p-AKT and p-ERK (Supplemental Figure 4C, D). Thus, bpAb-B/C and bpAb-B/D specifically inhibit downstream signaling by constitutively active FGFR2-fusion proteins.

We next assessed the ability of bpAb-B/C and bpAb-B/D to inhibit FGFR2-fusion driven oncogenic activity via focus formation assays using FGFR2-PHGDH transformed NIH3T3 fibroblasts (Figure 4I). Cells treated with bpAb-B/C and bpAb-B/D showed a dose-dependent decrease in transformation capacity (reduction in colony formation), whereas the parental antibodies and IgG1 treated control had no effect (Figure 4J). Collectively, these results highlight the specificity of the biparatopic antibodies towards FGFR2 and the marked improvement in the potency of FGFR2 inhibition when compared to bivalent monotopic antibodies.

Biparatopic antibodies show superior in vivo anti-tumor activity compared to the parental antibodies

We next tested the in vivo efficacy of bpAb-B/C and bpAb-B/D and their parental antibodies against subcutaneous tumors formed by FGFR2-PHGDH transformed BaF3 cells in SCID mice. At a tumor size of ~250mm^3, mice were randomized into 10 groups with 10 mice per treatment group. The antibodies were administered via intravenous tail vein injections twice per week for 4-6 weeks. Both bpAb-B/C and bpAb-B/D biparatopic

antibodies potently suppressed tumor growth at 5, 15, and 25mg/kg doses, whereas the parental antibodies (administered at 15 mg/kg) showed no anti-tumor activity (Figure 5A, B). Pharmacokinetics analysis by ELISA demonstrated dose-proportional increases in the plasma concentration of the biparatopic antibodies, and furthermore, considerably longer half-life compared to small molecule inhibitors, consistent with their larger size (29, 30) (Supplemental Figure 5A, B).

The biparatopic antibodies also showed prominent in vivo efficacy against xenograft tumors formed by the patient-derived, ICC13-7 cholangiocarcinoma model. While the parental antibodies had only marginal effects on tumor growth, the biparatopics were highly effective at both 10 and 30 mg/kg dose concentrations. Notably, bpAb-B/C showed greatest potency, resulting in tumor stasis at 38 days post-treatment (Figure 5C, D), comparable to the efficacies of clinically used FGFR inhibitors(28, 31). Importantly, bpAb-B/C and bpAb-B/D treatment in both in vivo models led to a marked decrease in total FGFR2 levels and reductions in p-FGFR, p-FRS2, and p-ERK compared to IgG1 control (Figure 5E, F, Supplemental Figure 5C, D). By contrast, the parental antibodies showed limited effect on total FGFR2 levels or on downstream signaling (Supplemental Figure 5E, F). Consistent with the tumor growth inhibition data, bpAb-B/C and bpAb-B/D markedly decreased tumor cell proliferation (Ki-67 staining) compared to parental antibodies or IgG1 control (Figure 5G, H). None of the antibody treatment affected mouse body weight (Supplemental Figure 5G, H). Assessment of antibody tumor distribution by IHC staining showed that bpAb-B/C and bpAb-B/D localized to the cell membrane and

exhibited diffuse staining throughout ICC13-7 xenografts (Supplemental Figure 5I), suggesting that biparatopic antibodies penetrate tumor effectively.

To investigate the potential involvement of immune effector functions mediated by biparatopic antibodies in ICC13-7 xenografts, we performed IHC staining for mouse NKp46, a marker for NK cell mediated antibody dependent cell-mediated cytotoxicity (ADCC) activation (32) and found no significant changes (Supplemental Figure 5J, K). Similarly, RNA sequencing analysis revealed minimal changes in murine gene expression across treatments except for the bpAb-B/C at 10mg/kg treatment group with only 4 immune-related genes upregulated (Supplemental Figure 5L). We further analyzed the immune system related gene sets and found no significantly differential expressed genes observed among treatment groups (Supplemental Figure 5N-Q). In all cases, tumor growths of matching bpAb-B/C and bpAb-B/D treated xenografts were substantially inhibited (Supplemental Figure 5M). Additionally, these antibodies were not potent inducers of NK cell killing of cancer cells (Supplemental Figure 5R), nor robust inducers of NFAT reporters via CD16 (ADC) or CD32a (antibody dependent cellular phagocytosis) in engineered Jurkat cells (Supplemental Figure 5S, T). Together these results demonstrate that bpAb-B/C and bpAb-B/D have improved anti-tumor activity compared to their parental antibodies in vivo likely driven by receptor down regulation.

Biparatopic antibodies promote receptor internalization and lysosomal degradation

We next explored the potential mechanism for FGFR2 downregulation by the biparatopic antibodies. To determine whether bpAb-B/C and bpAb-B/D promote FGFR2-fusion internalization, we treated FGFR2-PHGDH expressing BaF3 with bpAb-B/C, bpAb-B/D, or IgG control and then transferred cells to 4°C to block or 37°C to induce internalization. Surface levels of FGFR2 were analyzed by flow cytometry (Figure 6A, B). Cells treated with bpAb-B/C and bpAb-B/D showed increased internalization from 60-960 minutes (from ~6% to 80% shift in surface FGFR2) (Figure 6B). The internalization assay was repeated in ICC13-7 cells treated with bpAb-B/C, bpAb-B/D, respective parental antibodies, or IgG control. ICC13-7 cells treated with bpAb-B/C and bpAb-B/D had a significant decrease in surface FGFR2 compared to cells treated with parental antibodies B, C, or D or IgG1, suggesting that bpAb-B/C and bpAb-B/D enhanced FGFR2 receptor internalization (Figure 6C). Next, we labeled biparatopic and parental antibodies with a Fab fragment conjugated to a pH-sensitive fluorophore(33) and assessed lysosome-mediated induction of fluorescence in FGFR2-PHDGH, FGFR2-ACHYL1, and FGFR2-BICC1 expressing NIH3T3 cells (Figure 6D). Treatment with bpAb-B/C and bpAb-B/D resulted in marked increases in the fluorescent signal compared to the parental antibodies (Figure 6E-H). Labelling of lysosomes with lysotracker (green) and biparatopic antibodies with Fab-Fluor (red) demonstrated colocalization of the two signals, confirming the presence of the antibodies in the lysosomes (Supplementary Figure 6A). Consistent with results in FGFR2 fusion expressing NIH3T3 cells, treatment of the ICC13-7 cholangiocarcinoma cell line with bpAb-B/C and bpAb-B/D led to increases in fluorescent signals compared to parental antibodies (Figure 6I). In addition, bpAb-B/C and bpAb-B/D showed enhanced receptor internalization and degradation compared to parental

antibodies as well as parental antibodies mixtures confirming the unique mechanism of action of biparatopic antibodies beyond antibody combinations (Supplemental Figure 6C).

To investigate whether the observed increase in FGFR2 internalization is triggered by the intermolecular binding of antibodies, creating a large complex as shown in previous work (17, 34), we performed size exclusion chromatography coupled with multi-angle light scattering (SEC-MALS), to determine the mass of antibody and its complexes. Upon increasing the ratio of antigen (FGFR2 ECD) to the biparatopic antibody bpAb-B/C (ECD:Ab) from 1:1, 3:1, and 5:1, SEC-MALS data showed absolute masses consistent with higher-order complexes (Supplemental Figure 6B, see predicted complexes). These results suggest that the bpAb-B/C biparatopic antibodies bind to FGFR2 receptors in trans likely creating larger antibody-receptor complexes leading to more rapid internalization.

To determine whether the internalization and receptor downregulation are mediated by lysosomal degradation, we suppressed lysosome acidification and catabolism using the vacuolar-type H+-ATPase inhibitor bafilomycin A1 (BafA1). Bafilomycin treatment rescued bpAb-B/C- or bpAb-B/D-induced FGFR2-OPTN downregulation in ICC13-7 as compared to IgG1 treated control (Figure 6J, Supplemental Figure 6D). Together, these data demonstrate that bpAb-B/C and bpAb-B/D induce FGFR2-fusion internalization, trafficking, and lysosomal-mediated degradation to decrease FGFR2 fusion driven activity and growth. Notably, this mode of action induced by the biparatopic antibodies as shown in our work and others (17, 35–37), does not require co-targeting of lysosome-targeting

receptors, membrane E3 ligases, or autophagy signaling molecules as seen in the development of LYTAC, AbTAC, or AUTAC systems(38).

Biparatopic antibodies potentiate the efficacy of FGFR inhibitors

Given the specificity of FGFR2 antibodies and the potency of FGFR1-3 kinase inhibitors, combining two distinct treatment modalities might result in cooperativity specific to FGFR2 while sparing FGFR1 and 3, leading to more potent FGFR2 inhibition. To test whether bpAb-B/C and bpAb-B/D synergize with FGFRi, FGFR2-PHGDH expressing BaF3 cells were treated in a titration matrix of bpAb-B/C or bpAb-B/D in combinations with approved FGFRi infigratinib, futibatinib, and pemigatinib. The Bliss model was then applied to determine the degree of synergy (39). Bliss scores of 0-10 generally indicate additive interactions, while scores >10 demonstrate synergistic interactions. In the absence of FGF10, combination of bpAb-B/D with infigratinib, pemigatinib, or futibatinib as well as combination of bpAb-B/C with futibatinib or pemigatinib moderately enhanced growth inhibition (Figure 7A, B). Synergy between bpAb-B/C and infigratinib in a ligand-independent setting was striking, with a Bliss score of >20 (Figure 7B, C). In the presence of FGF10, co-treatments of bpAb-B/C or bpAb-B/D with infigratinib, futibatinib, and pemigatinib all enhanced growth suppression compared to treatment with single agents (Figure 7A-C). In accordance with the dose-response, all Bliss values were well above 10 in the ligand-dependent context (Figure 7C). These data highlight the potential of the biparatopic antibodies to boost the activity of FGFR inhibitors both in the presence and absence of ligand.

Diverse secondary FGFR2 kinase domain mutations drive clinical resistance to each of each FGFR TKI studied to date (3, 40, 41). Given the intracellular location of the kinase domain, we hypothesized that the biparatopic antibodies might remain active against these mutations. To test this hypothesis, we selected the gatekeeper mutations V565I and V565F, which are common mechanisms of resistance to the approved FGFR inhibitors. NIH3T3 cells stably expressed FGFR2-ACHYL1 with a V565I or V565F mutation were resistant to infigratinib (Supplemental Figure 7A) but were sensitive to bpAb-B/C and bpAb-B/D, showing inhibition of both growth (Figure 7D, E) and downstream signaling; p-FGFR, p-FRS2, and p-ERK1/2 (Figure 7F, Supplemental Figure 7B). Moreover, bpAb-B/C or bpAb-B/D induced lysosomal degradation of the FGFR2 fusion in these cells as assayed by anti-Fc Fab fragment conjugated pH-sensitive fluorophore (Figure 7G, H), similar to that observed in NIH3T3 cells expressing the initial FGFR2 fusions (Figure 6F-H). Given the complexity of resistance mechanisms in patient tumors, which may implicate multiple oncogenes and bypass mechanisms, we modeled the efficacy of our antibodies in the FGFR1-dependent cholangiocarcinoma cell line, CCLP-1, stably transduced to express the FGFR2-PGHDH WT or FGFR2-PHGDH-V565F alleles (Supplemental Figure 7C, D). CCLP-1 parental cells as well as CCLP-1 cells expressing FGFR2-PHGDH WT were sensitive (IC50<2nM), while FGFR2-PHGDH V565F cells were resistant (IC50>2000 nM) to infigratinib (Supplemental Figure 7E). To determine the dose of infigratinib to use in combination studies (in order to suppress the concurrent FGFR1 activity), we determined the infigratinib concentration that sensitized cells expressing FGFR2-PHGDH WT but not FGFR2-PHGDH V565F (0.15uM). Treatment with bpAb-B/C or bpAb-B/D in combination with infigratinib significantly

suppressed growth of V565F resistant mutants and re-sensitized the CCLP-1 resistant cells to infigratinib, indicating robust suppression of the introduced FGFR2 resistance allele (Figure 7I). In addition, co-treatments of infigratinib and bpAb-B/C or bpAb-B/D decreased levels of FGFR2, p-FGFR, p-FRS2, and p-ERK1/2 (Figure 7J, Supplemental Figure 7F). These results support the use of bpAb-B/C and bpAb-B/D to overcome secondary FGFR2 kinase domain mutations.

In addition to FGFR2 rearrangements, a recent study revealed that activating in-frame FGFR2 ECD deletions occur in ~3% of ICC patients. Patients with these FGFR2 ECD deletions responded well to FGFRi treatments, suggesting that these ECD mutations are oncogenic drivers(42). Since these mutations are located in the ECD, it is possible that they might lack sensitivity to our biparatopic antibodies. To determine whether bpAb-B/C or bpAb-B/D have activity against oncogenic FGFR2 ECD in-frame deletion mutations, we engineered NIH3T3 cells to stably express 4 patient-derived FGFR2 ECD deletion mutations (Figure 7K). Compared to NIH3T3 cells expressing FGFR2-WT, cells expressing deletion mutations had increased transformation capacities and receptor dimerization as analyzed by soft-agar assay and NanoBiT assays, respectively (Supplemental Figure 7G-K). In addition, the ECD mutants had elevated FGFR2 downstream phosphorylation; p-FGFR, p-FRS2, and p-ERK1/2, which was blocked by infigratinib, confirming their FGFR2 dependency (Supplemental Figure 7L, M). While bpAb-B/C or bpAb-B/D had moderate activities against patient 1 and 3- derived mutants, to our surprise, both bpAb-B/C and bpAb-B/D effectively inhibited growth of patient 2 and 4 variants (Figure 7L). These results correlated with the decrease in levels of FGFR2, p-

FGFR, p-FRS2, and p-ERK1/2 for the H167_N173Del (patient 2) variant (Figure 7M, Supplemental Figure 7O). Importantly, levels of FGFR2 decreased upon bpAb-B/C and bpAb-B/D treatments, suggesting that receptor internalization and degradation mediate the observed growth inhibition (Figure 7M, Supplemental Figure 7O). Crucially, mutations found in patients 1-4 are predicted to alter the three-dimensional structure of FGFR2 D2 and D3 domains (42) and may consequently affect the binding affinities of bpAb-B/C and bpAb-B/D with D1 and D2 binding arms. Nevertheless, the fact that bpAb-B/C and bpAb-B/D remain effective against patient 2 and 4 variants suggest that as long as the binding avidities of D1 and D2 binders are sufficient to establish intermolecular interaction and trigger internalization, the bpAb-B/C and bpAb-B/D should be effective. These data demonstrate that bpAb-B/C and bpAb-B/D have activities against intracellular kinase domain mutations and specific patient-derived FGFR2 ECD oncogenic deletions. Together with the observed synergy, these data support the notion of combining FGFR1-3 inhibitors with FGFR2 biparatopic antibodies.

DISCUSSION

In this study, we established that the FGFR2 ECD is required for the oncogenic activity of FGFR2 fusions. A series of monospecific antibodies against FGFR2, however, were largely ineffective at blocking downstream signaling. Accordingly, we systematically generated biparatopic antibodies against a diverse combination of epitopes that span three domains on the FGFR2 ECD. Through unbiased phenotypic screening using cancer growth inhibition as a functional readout, we selected two biparatopic antibody candidates that achieved highest efficacy in vitro and confirmed their therapeutic activities in FGFR2

fusion ICC xenograft models in vivo. The antibodies had synergistic combination activity with FGFR2 TKIs and had activity against gatekeeper kinase mutations as well as N-terminal oncogenic FGFR2 alterations in the ECD. Overall, our work highlights the therapeutic potential of these antibodies in ICC and presents a framework for the development of biparatopic antibodies more broadly.

A variety of modes of action of biparatopic antibodies might contribute to their efficacy. Upon binding to its target, the biparatopic antibody could 1) exert agonistic activity by mimicking the ligand-induced receptor activation(43), 2) act as a true ligand-antagonist blocking the ligand interaction and downstream signaling activation, or 3) induce receptor internalization and degradation through intermolecular crosslinking and complex formation. Critically, only the latter mode of action can inhibit ligand-independent receptor activation and sustainably downregulate signaling pathway to reduce tumor growth. In this work, we have shown mechanistically that the abilities of bpAb-B/C and B/D to effectively inhibit ligand-independent FGFR2 fusion activation are likely mediated through enhanced receptor internalization and lysosome-mediated receptor degradation, which results in tumor growth inhibition in vivo.

Recent advances have been made in the field of targeted protein degradation utilizing endo-lysosomal pathways, such as lysosome-targeting chimeras (LYTACs) and antibody-based PROTAC (AbTAC) platforms. Despite their promises for eliminating soluble proteins, the success of these platforms at targeting membrane receptors relies on the endogenous trafficking kinetics of specific RTKs, lysosome targeting receptors, or

transmembrane E3 ligases involved as well as their expression and colocalization(44, 45). Moreover, such antibodies require further modifications beyond the standard IgG format. Biparatopic antibodies, on the other hand, can be systematically designed against receptors such that the specific epitope combinations can promote receptor binding, trafficking, and degradation of target receptors (17, 35–37). If such antibodies can achieve comparable target degradation, they would be accompanied by the advantages of a standard IgG format, including long half-life, high specificity, ability to recruit effector functions, and low immunogenicity(46). Thus, the rational engineering and screening of biparatopic antibody platforms may provide a simple yet powerful approach to target a broad range of receptor oncogenes.

Acquired secondary mutations in the FGFR2 kinase domain are an important mechanism of resistance to FGFR TKIs. Although next-generation covalent FGFR TKIs with broader spectrum activity against these mutations have been developed, on-target resistance remains a major limitation to monotherapy with these agent (3). We provide proof-of-concept data that biparatopic antibodies bpAb-B/C and bpAb-B/D targeting the FGFR2 ECD can overcome various kinase domain resistance in FGFR2 fusions. Indeed, previous studies have leveraged antibody or antibody combinations to overcome acquired resistance in other cancer settings, such as in the case of EGFR(47, 48). Thus, biparatopic antibodies with high activity and low toxicity have the therapeutic potential to target various forms of RTK resistance to small molecule kinase inhibitors.

We and others have shown that dual inhibition of oncogenes using two targeted agents having non-overlapping patterns of cross-resistance can delay or prevent the occurrence of on-target resistance(49, 50). Specifically, dual targeting of BCR-ABL oncogene with a combination of allosteric and catalytic ABL inhibitors acting at distinct sites are non-cross resistant and eradicate CML tumors in preclinical models(50). Similarly, based on the observed synergy between bpAb-B/C and bpAb-B/D and FGFR inhibitors (Figure 7) we speculate that combination treatments of FGFR2 biparatopic antibodies and pan-FGFR inhibitors might delay or prevent the emergence of acquired resistance. A considerable advantage of highly active antibodies is the relative ease of combining such agents with small molecule inhibitors, as it has often been difficult to create well-tolerated combinations of targeted agents.

In all, our work has uncovered potent FGFR2 biparatopic antibodies as potential targeted treatment for FGFR2-driven ICC. Our results demonstrated that the engineering of biparatopic antibodies has the potential to lead to more effective and targeted treatments for a wide range of cancers.

METHODS

Sex as a biological variable

Our study exclusively examined female mice because the female mice tend to engage in less aggressive behavior including fighting, compared to their males. Similar phenotypes are reported in FGFR2 driven models in both sexes.

Generation of DNA constructs and cell lines

FGFR2-ACHYL1(2), *FGFR2-BICC1*(2), and *FGFR2-PHGDH*(3) sequences were previously described as referenced. *FGFR2-ACHYL1* and *FGFR2-BICC1* constructs were synthesized (Genscript) and cloned into MSCV vector (addgene: #24828). *FGFR2* ECD with Ig subdomain deletions were generated based on *FGFR2-BICC* full-length sequence without AA37(Glu)-AA126(Asp) in Ig1 (D1), AA154(Pro)-AA247(Asp) in Ig2 (D23), AA250(Glu)-AA361(Gln), and AA154(Pro)-AA361(Gln) in Ig2-3 (D2+3) deletion constructs. All the mutant constructs were cloned into pBabe-puro-gateway via Gateway cloning strategy (addgene: #51070). All construct maps were sequence validated and aligned using SnapGene software.

To generate isogenic cell lines expressing FGFR2 fusions, retrovirus was generated by transfecting Platinum-E (Plat-E) retroviral packaging cell line (Cell Biolabs). For FGFR2 ECD WT and mutants, NIH3T3 (ATCC) and HEK-293T cells (ATCC) were transiently transfected with *FGFR2-BICC1* or its variants. 6 parental antibodies and anti-human IgG1-FITC (Jackson Lab, Catalog#709-545-098) were used as primary and secondary

antibodies respectively to validate the Ig-specific deletion mutants. Analysis was done using FlowJo v.10.8 software. ICC13-7 and CCLP-1 cholangiocarcinoma patient-derived cell lines were gifts from the Bardeesy lab (N.B., Massachusetts General Hospital Cancer Center, Boston, MA) and were authenticated via STR profiling.

Biparatopic antibodies design and generation

6 Parental antibody sequences were synthesized from the referenced sequences (Table. S1). To generate biparatopic antibodies, controlled Fab arm exchange reactions were performed where F405L and K409R containing antibodies were mixed in an equimolar ratio according to the protocol(27). Immediately following the incubation period, the antibodies were buffer exchanged into PBS using a PD-10 desalting column (GE Healthcare) to remove the 2-MEA. To assess the quality and concentration of the bispecific antibodies, SDS-PAGE, SEC-HPLC and Mass Spectrometry analysis were performed.

Dimerization Assay

For NanoBiT constructs, *FGFR2-WT, FGFR2-ACHYL1* and *FGFR2-BICC1* were C-terminally tagged with Small BiT or Large BiT derived from NanoLuc (Promega). Full-length sequences were cloned into a pLenti and pLX304 retroviral vectors with puromycin and blasticidin selection markers respectively. HEK293T cells were stably or transient transfected using TransIT®-LT1 Transfection Reagent. 24-30 h after transfection, Nanoluc substrate (Nano-Glo® Live Cell, Promega, Cat#N2011) was added the mixture

was incubated at 37 degrees for 15 minutes according to the manufacturer protocol. The luciferase activity was measured by EnVision plate reader (PerkinElmer).

Immunohistochemistry

Tumors were surgically removed and placed in 10% neutral buffered formalin for 24 h and followed by 70% ethanol until paraffin embedded. Immunohistochemistry was performed by Histowiz. Antibodies, anti-Ki67 (Abcam, Catalog#ab15580), anti-IgG1 (Abcam, Catalog# ab109489), and anti-mNKp46 (R&D, Catalog# AF2225) were used at 1:100 dilution and hematoxylin solution were used for counterstaining.

Immunoblotting

Cell lysates in RIPA buffer (50mM Tris pH 7.4, 150mM NaCl, 1% NP-40, 0.5% sodium deoxycholate and 0.1% SDS) were resolved on 8% or 4-20% Tris-Glycine gels and transferred to PVDF membranes (Novex). The following antibodies were used as primary antibodies at 1:1000 dilution and were obtained from Cell Signaling Technologies:
AKT (Catalog#2920), pAKT (S473) (Catalog#4060), ERK1/2 (Catalog#4695), pERK1/2 (T202/Y204) (Catalog#9106), pFGFR (Y653/654) (Catalog#3471), pFRS2(Y436) (Catalog#3861), pFRS2(Y196) (Catalog#3864), GAPDH (Catalog#97166), MEK1/2 (Catalog#4694), pMEK1/2 (S217/221) (Catalog#9154), Tubulin (Catalog#3873), and from Genscript: FGFR2 (parental antibody E), Abcam: FRS2(Catalog#ab183492), and Sigma Aldrich: Vinculin (Catalog#V9131).

Transformation Assays

Focus formation assay: NIH3T3 stably expressing FGFR2 fusions were plated at $5x10^5$cells per well in 6-well plate in triplicate. Cells were grown for 7-10 days, plates were imaged, and the number of foci were blindly counted. *Soft agar colony formation assays*: NIH3T3 cells stably expressing patient-derived oncogenic FGFR2 variants were plated at $1x10^4$ cells per well in 6 well-plates with 0.5% Select Agar (ThermoFisher Catalog# 30391049). Cells were cultured for 2-3 weeks, and colonies were imaged, and colony numbers were determined using ImageJ and Prism software.

BaF3 transformation assay: BaF3 cells (Creative Bioarray) were resuspended in RPMI media + 10%FBS with 0% IL-3. Cells were seeded at 20,000 cells per well in 6-well plate and were split every 3 days. For each split, Cell-titer Glo was used to measure the cell viability compared to original seeding density and the new seeding density was determined. Cumulative population doublings were calculated at each split from $\log_2$(current density/previous density/split) over the period of 15-20 days. All antibodies were added to a final concentration of 2 µM and were replaced every 3 days during each passage.

Binding affinity and epitope binning assays

MSD-SET (Meso Scale Discovery-Solution Equilibrium Titration)

Measurements were performed according to the previously published protocol(51). Briefly, in a 96 well assay plate, a constant concentration of antibody is incubated with titrating concentrations of antigen in an assay buffer PBS 1x pH7.4, 0.1% BSA (Sigma-Aldrich) w/v, 0.02% P20 (ThermoFischer). Once the antibody-antigen interaction is reached, the free antibody is transferred and quantified by allowing it to incubate on an

antigen-coated MSD plate MSD (PN: L15XA-3). Then, subsequent detection with an ECL-labeled secondary antibody was performed. Experiments were performed as independent duplicates.

BLI-Octet (Bio-Layer Interferometry)

Binding kinetics (ka, kd) and affinity (Kd) were measured in an Octet system RED96e at 25 °C with shaking at 1,000 rpm using 1x kinetic buffer (Sartorius; PN: 18-1105). Antibodies were captured by Anti-Human Fc capture biosensor (AHC) (Sartorius, PN: 18-5060) for 300 s at 0.5 ug/mL. hFGFR2 ECD 22-378 His-tag (SinoBiological; PN: 16485-H08H) was used as an analyte, with seven 2-fold dilutions from 100nM using DFx2. Association and dissociation of the analyte to the captured antibody was monitored for 300 s and 600 s, respectively. Data were analyzed using the Octet Data Analysis software HT 12.0. Sensorgrams were fitted to a 1:1 binding model where kinetic rate Ka and Kd were globally fitted.

Epitope binning

Epitope binning experiments were performed in an Octet system RED96e at 25 °C with shaking at 1,000 rpm using 1x kinetic buffer (Sartorius; PN: 18-1105). To perform an in tandem epitope binning experiment, biotinylated hFGFR2 ECD AA22-AA378 His-tag (SinoBiological; PN: 16485-H08H) was captured on streptavidin sensor (SA) (Sartorius; PN: 18-5020) for 300s at 1ug/mL concentration. hFGFR2 was biotinylated using Abcam Biotinylation Kit (PN: ab201796). The cycle starts with the capturing of biotinylated ligand followed by a “primary” antibody (Ab1) binding step where Ab1 interaction is monitored

for 600s at 333nM concentration. Shortly after, a “competing” antibody (Ab2) interaction is monitored for 300s at 333nM concentration. All antibodies are used at a concentration >10*Kd to ensure ligand saturation. Data were blindly analyzed using the Octet Data Analysis software HT 12.0 and R Studio “pvclust” according to Octet Application note n.16.

Avidity measurement

NIH3T3 cells expressing FGFR2-PHGDH were resuspended at a concentration of $8.0x10^7$ cells/mL and seeded on z-Movi (LUMICKS Inc) microfluidic chips that were coated with Poly-L-Lysine (Sigma, P4707). Z-Movi chips seeded with 3T3 cells were placed in a 37°C dry incubator for at least 2 h for attachment. 20uL of antibody-on-beads were flowed onto the z-Movi chip and incubated with the target 3T3 cells for 30 seconds. Following incubation, an acoustic force ramp from 0 to 1000 pN over 2:30 minutes was applied within the z-Movi chip and antibody-on-bead detachment was observed using real-time fluorescence imaging on the z-Movi system. Each z-Movi chip was used to sequentially flow in negative control, parental antibody pair, and corresponding biparatopic antibody-coated beads. Replicates were performed on different z-Movi chips with randomized run orders for antibody conditions. Avidity experiments were processed using proprietary Oceon software.

Flow cytometry

Apparent affinity analysis: $1x10^6$ of NIH3T3 cells expressing full-length and FGFR2-BICC1 variants (D1, D2, D3, or D2+D3 deletion variants), SNU-16 cells, or parental BaF3

cells (neg control) per tube were incubated with parental antibody A-F at final concentration of 10ug/mL (NIH3T3) or at serial dilutions of 0, 1ng/mL, 10ng/mL, 50ng/mL,100ng/mL, 1mg/mL, 10mg/mL (SNU-16) in 1xPBS (Mg^{2+} free) for 1.5 h at room temperature (52). Cells were washed three times with FACS buffer (1xPBS, 1% BSA, 5% FBS) and incubated with goat anti-human IgG Alexa Fluor 488 (Jackson ImmunoResearch, Catalog#109-545-098) secondary antibody for 30mins, washed, and analyzed on a SA3800 Spectral Analyzer (Sony Biotechnology). Data were analyzed using FlowJo® v.10 software and fit in GraphPad Prism 9 using a ligand-binding quadratic equation to obtain K_d values.

Antibody internalization assay

$7.5x10^5$ of BaF3 cells expressing FGFR2-PHGDH were distributed in each tube for each condition. All antibodies were added to wells at a final concentration of 5 µg/mL in serum-free RPMI media and incubated for 1 h on ice. After washing to remove excess antibodies, cells were transferred to 4°C or 37°C for 1, 2, 3, 4 and 16 h, then washed three times with FACS buffer. Surface FGFR2-bound parental or biparatopic antibodies were detected with goat anti-human IgG Alexa Fluor 488 secondary antibody and analyzed on a CytoFLEX S (Beckman Counter). The geometric mean of signal per sample determined using FlowJo® v.10 software.

Fabfluor receptor degradation

NIH3T3 or ICC13-7 cells were seeded at 7500 cells per well in 96 well-plate (Corning, Catalog#3595). Red Incucyte® Fabfluor-pH Antibody Label reagents (Sartorius, Catalog#4722)(33) stock concentration at 0.5mg/mL were mixed and incubated with each antibody at 1:3 molar ratio of antibody:Fabfluor label for 30 mins at 37°C. Antibody-

Fabfluor label mix were added to the cells at 4ug/mL final concentration. Images were taken by Incucyte at 20X every 30 mins for up to 72 h. Analysis was done using Incucyte Basic Analyzer with Top-Hat background subtraction. Red Total Integrated Intensity Per Well (RCU/OCU x μm^2 /Well) was quantified as a readout using Incucyte software v2019B.

Growth inhibition Assay

Engineered BaF3 cells expressing FGFR2-PHGDH and FGFR2-ACHYL1 cells were seeded at 7500 cells/well in 0% IL3, RPMI + 10%FBS media in 96 well-plates (Corning, Catalog#3904). Parental antibodies, biparatopic antibodies, or IgG1 control (Bio X Cell, Catalog#BP0297) were added 24 h post seeding at 15 serial concentrations ranging from 0 to 1uM. For viability assay in the presence of FGF10, FGF10 (R&D Systems, Catalog# 345-FG-025) were added 4 h after the antibody treatment at a final concentration of 100ng/mL. Viability was determined using CellTiter-Glo™ 2.0 (Promega) at day 5 post treatment according to the manufacturer's instructions.

ADCC and ADCC activity assays

For *NK cell killing assay,* ICC13-7 were seeded into 96-well black-clear bottom plates (Corning) at 5,000 cells per well. IncuCyte CytoLight Rapid Green Reagent (Essen BioScience, CAT#4705) was added to each well at a concentration of 330 nM for cytoplasmic labeling, and cells incubated overnight. Engineered NK-92 cells (53) were added to each well in 50 µL of MyeloCult™ H5100 medium (STEMCELL) with 12.5% heat-inactivated horse serum (Gibco) and 100 units/mL human recombinant IL-2

(PeproTech, Catalog#AF-200-02). FGFR2 biparatopic antibodies or an IgG control were added in 50 µL of the same medium, containing IncuCyte Annexin V Red (Essen BioScience, Catalog#4641, 1:500) and was imaged using IncuCyte S3 (Essen BioScience). For *ADCC and ADCP reporter assays*, ICC13-7 were seeded 5000 cells per well with Jurkat-NFAT-hCD16 (ADCC) and Jurkat-NFAT-hCD32 cells (ADCP) (InvivoGen, Catalog# jktl-nfat-cd16, jktl-nfat-cd32) at 20,000 cells for 24 h, QUANTI-Luc™ 4 Reagent were added, and the plate were analyzed in EnVision.

Mouse xenograft experiments

$5x10^6$ of BaF3 cells expressing FGFR2-PHGDH or $3x10^6$ of ICC13-7 cells in a total volume of 200uL (100uLMatrigel + 100uL PBS) were subcutaneous implanted in the right flank of 7–9-week-old female BALB/c scid mice (Jackson Laboratory, strain#001803). At a tumor size of ~250mm^3 (BaF3) or ~150mm^3 (ICC13-7), mice were randomized into 10 groups, 10 mice per treatment group. Biparatopic antibodies, parental antibodies, or IgG1 (Bio X Cell, Catalog#BP0297) were IV administered twice per week and tumor sizes were measured by caliper every 3-4 days for 25 days (BaF3) and 38 days (ICC13-7). Tumor volume was calculated by the modified ellipsoidal formula: $V = 0.523 \times (L \times W^2)$ where L = the greatest longitudinal diameter and W = the greatest transverse diameter (width). One-way ANOVA multiple comparisons (Friedman's ANOVA multiple comparisons) statistical analysis was used to compare tumor sizes among all paired groups.

All experiments were conducted under protocol 0121-09-16-1 approved by the Broad Institute's Institutional Animal Care and Use Committee (IACUC).

RNA sequencing analysis

Tumors were surgically removed, flash frozen in liquid nitrogen, and processed for RNA sequencing (Azenta). A combined human-mouse genome reference was constructed and RNA-seq reads from samples were aligned to this integrated genome using STAR aligner (54). Feature Counts was used to quantify reads mapped specifically to mouse-derived genes, providing gene-level counts. For differential expression analysis (DEG), edgeR package was used (55) . After obtaining raw p-values for each gene, we applied False Discovery Rate (FDR) correction to control for multiple testing, resulting in a list of significant DEGs with adjusted p-values.

To estimate overall ADCC, ADCP, and CDC pathway activity, we selected five GO terms: 0002228, 0001788, 0002431, 0002281, 0002430. The overall activity score was calculated by taking a weighted sum of the gene expression values within each GO term (assigning equal weights of 1 to each gene) and dividing by the total sum of weights. IgG1 group was used as a reference and t-tests were conducted to determine whether any GO term activity score in different treatment groups differed significantly from this control group. We applied FDR correction to p-value to adjust for multiple comparisons, resulting in adjusted p-values.

ELISA assay

Blood samples were collected from the submandibular veins of mice at 1, 24, and 72 h post the last dose of the treatment before the harvest. Levels of plasma antibody were measured with the Human IgG Total ELISA Kit (Sigma Aldrich) per manufacturer's instructions. The absorbance was measured with EnVision (PerkinElmer).

Phospho-receptor tyrosine kinase profiling

Protein was prepared per protocol (Human Phospho-RTK Array Kit, Catalog #ARY001B): Cells starved of FBS and treated with antibodies (1 uM) for 5 h. Cells were harvested in lysis buffer provided in kit with protease and phosphatase inhibitors added before use. Membranes were exposed to X-ray film (Fuji) for multiple exposure times and dots were mapped using reference spots provided and analyzed for relative intensity using ImageJ.

Statistics:

All statistical analyses were performed using GraphPad Prism 9.0 or 10.0. Data are reported as mean ± SEM. One-way ANOVA multiple comparisons was used to calculate P values for comparisons of 3 or more groups. Friedman's ANOVA multiple comparisons were used to compared between treatment groups in xenograft experiments. Samples analyzed from in vivo experiments were randomly selected with no exclusion criteria. P values of less than 0.05 were considered significant. Statistical parameters can be found in the figure legends.

Study approval:

All in vivo experiments were conducted under protocol 0121-09-16-1 approved by the Broad Institute's Institutional Animal Care and Use Committee (IACUC).

Data Availability:

RNA sequencing data was deposited with GEO accession number: GSE281992. The unedited blots are provided as an individual file that is part of the supplemental material.

Values used for graphs in figures and reported means are provided in the Supporting Data Values file in the supplemental material.

Acknowledgements:

We thank Drs. James Cleary for information regarding FGFR2 ECD mutations and Song-My Hoang of Lumicks for avidity analysis. We thank the members of the Flow Cytometry Core Facility at the Broad Institute for cell analysis and the Comparative Medicine Department at the Broad institute for animal care. Some figures were generated using Biorender

This work was supported by grants from the US Department of Defense, Congressionally Directed Medical Research Programs (CDMRP), Peer Reviewed Cancer Research Program Translational Team Science Award (W81XWH-21-PRCRP-TTS, N.B and W.R.S), the Department of Defense CDMRP Peer Reviewed Cancer Research Program (PRCRP) Horizon Award (W81XWH-20-1-0325 to S.C.), and the Cholangiocarcinoma Foundation fellowship (Andrea Lynn Scott Memorial Research Fellowship to S.C.). Ridgeline Discovery (W.R.S) and NCI R01CA233626 (W.R.S).

Author contributions:

S.C. and W.R.S. conceived, designed, analyzed the experiments, and wrote the manuscript. S.C., S.O., D.T.F., J.K., F.P.R., T.Y.S., Y.C.C. and M.C. performed antibody validations, in vitro activity assays, and mechanistic validation experiments. A.S., S.C. characterized antibody binding epitopes and affinities. J.K., S.C., D.J.R., L.C., performed

in vivo xenografts experiments. D.K. provided antibody-antigen structural insights. D.T.F., J.K., A.A., R.D., Y.Y.T., Y.H., processed and analyzed xenograft-derived samples. N.B. provided ICC models and critical insights into ICC biology and FGFR inhibitors. All authors reviewed and edited the manuscript.

REFERENCES

1. Borad MJ, Gores GJ, Roberts LR. Fibroblast growth factor receptor 2 fusions as a target for treating cholangiocarcinoma. *Curr Opin Gastroen*. 2015;31(3):264–268.

2. Arai Y, et al. Fibroblast growth factor receptor 2 tyrosine kinase fusions define a unique molecular subtype of cholangiocarcinoma. *Hepatology*. 2014;59(4):1427–1434.

3. Goyal L, et al. TAS-120 Overcomes Resistance to ATP-Competitive FGFR Inhibitors in Patients with FGFR2 Fusion–Positive Intrahepatic Cholangiocarcinoma. *Cancer Discov*. 2019;9(8):1064–1079.

4. Goyal L, et al. Futibatinib for FGFR2-Rearranged Intrahepatic Cholangiocarcinoma. *New Engl J Med*. 2023;388(3):228–239.

5. Chen L, et al. Fibroblast growth factor receptor fusions in cancer: opportunities and challenges. *J Exp Clin Canc Res*. 2021;40(1):345.

6. Borad MJ, et al. Updated dose escalation results for ReFocus, a first-in-human study of highly selective FGFR2 inhibitor RLY-4008 in cholangiocarcinoma and other solid tumors. *J Clin Oncol*. 2023;41(16_suppl):4009–4009.

7. Maadi H, et al. The effects of trastuzumab on HER2-mediated cell signaling in CHO cells expressing human HER2. *Bmc Cancer*. 2018;18(1):238.

8. Clynes RA, et al. Inhibitory Fc receptors modulate in vivo cytoxicity against tumor targets. *Nat Med*. 2000;6(4):443–446.

9. Grugan KD, et al. Fc-mediated activity of EGFR x c-Met bispecific antibody JNJ-61186372 enhanced killing of lung cancer cells. *Mabs*. 2017;9(1):114–126.

10. Zinn S, et al. Advances in antibody-based therapy in oncology. *Nat Cancer*. 2023;4(2):165–180.

11. Carter PJ, Lazar GA. Next generation antibody drugs: pursuit of the “high-hanging fruit.” *Nat Rev Drug Discov*. 2018;17(3):197–223.

12. Mijares A, et al. From Agonist To Antagonist: Fab Fragments of an Agonist-Like Monoclonal Anti-β2-Adrenoceptor Antibody Behave as Antagonists. *Mol Pharmacol*. 2000;58(2):373–379.

13. Prat M, et al. Agonistic monoclonal antibodies against the Met receptor dissect the biological responses to HGF. *J Cell Sci*. 1998;111(2):237–247.

14. Merchant M, et al. Monovalent antibody design and mechanism of action of onartuzumab, a MET antagonist with anti-tumor activity as a therapeutic agent. *Proc National Acad Sci*. 2013;110(32):E2987–E2996.

15. Ettenberg SA, et al. Inhibition of tumorigenesis driven by different Wnt proteins requires blockade of distinct ligand-binding regions by LRP6 antibodies. *Proc National Acad Sci*. 2010;107(35):15473–15478.

16. Meric-Bernstam F, et al. Zanidatamab, a novel bispecific antibody, for the treatment of locally advanced or metastatic HER2-expressing or HER2-amplified cancers: a phase 1, dose-escalation and expansion study. *Lancet Oncol*. 2022;23(12):1558–1570.

17. Weisser NE, et al. An anti-HER2 biparatopic antibody that induces unique HER2 clustering and complement-dependent cytotoxicity. *Nat Commun*. 2023;14(1):1394.

18. Reyes-Alcaraz A, et al. A NanoBiT assay to monitor membrane proteins trafficking for drug discovery and drug development. *Commun Biology*. 2022;5(1):212.

19. Olsen SK, et al. Insights into the molecular basis for fibroblast growth factor receptor autoinhibition and ligand-binding promiscuity. *Proc National Acad Sci*. 2004;101(4):935–940.

20. Ito T, et al. Paralog knockout profiling identifies DUSP4 and DUSP6 as a digenic dependence in MAPK pathway-driven cancers. *Nat Genet*. 2021;53(12):1664–1672.

21. Leung GP, et al. Hyperactivation of MAPK Signaling is Deleterious to RAS/RAF Mutant Melanoma. *Mol Cancer Res*. 2018;17(1):molcanres.0327.2018.

22. SETH E, et al. ANTIBODY DRUG CONJUGATES.

23. AXEL H, et al. ANTI-FGFR2 ANTIBODIES AND USES THEREOF.

24. YIYUAN Y, et al. ANTI-FGFR2/3 ANTIBODIES AND METHODS USING SAME.

25. JIN KK, et al. MONOCLONAL ANTIBODIES TO FIBROBLAST GROWTH FACTOR RECEPTOR 2.

26. Smyth EC, et al. Trial in progress: Phase 3 study of bemarituzumab + mFOLFOX6 versus placebo + mFOLFOX6 in previously untreated advanced gastric or gastroesophageal junction (GEJ) cancer with FGFR2b overexpression (FORTITUDE-101). *J Clin Oncol*. 2022;40(16_suppl):TPS4164–TPS4164.

27. Labrijn AF, et al. Controlled Fab-arm exchange for the generation of stable bispecific IgG1. *Nat Protoc*. 2014;9(10):2450–63.

928 28. Wu Q, et al. EGFR Inhibition Potentiates FGFR Inhibitor Therapy and Overcomes
929 Resistance in FGFR2 Fusion-Positive Cholangiocarcinoma. *Cancer Discov*.
930 2021;12(5):1378–1395.

931 29. Sootome H, et al. Futibatinib Is a Novel Irreversible FGFR 1–4 Inhibitor That Shows
932 Selective Antitumor Activity against FGFR-Deregulated Tumors. *Cancer Res*.
933 2020;80(22):4986–4997.

934 30. Liu PCC, et al. INCB054828 (pemigatinib), a potent and selective inhibitor of
935 fibroblast growth factor receptors 1, 2, and 3, displays activity against genetically
936 defined tumor models. *Plos One*. 2020;15(4):e0231877.

937 31. Subbiah V, et al. RLY-4008, the first highly selective FGFR2 inhibitor with activity
938 across FGFR2 alterations and resistance mutations. *Cancer Discov*. [published online
939 ahead of print: 2023]. https://doi.org/10.1158/2159-8290.cd-23-0475.

940 32. Sivori S, et al. p46, a Novel Natural Killer Cell–specific Surface Molecule That
941 Mediates Cell Activation. *J Exp Med*. 1997;186(7):1129–1136.

942 33. Bevan NJ, Dale TJ, Trezise DJ. Abstract 749: Antibody internalization assays for
943 cancer drug discovery. *Cancer Res*. 2018;78(13_Supplement):749–749.

944 34. Spangler JB, et al. Combination antibody treatment down-regulates epidermal
945 growth factor receptor by inhibiting endosomal recycling. *Proc Natl Acad Sci*.
946 2010;107(30):13252–13257.

947 35. DaSilva JO, et al. A Biparatopic Antibody–Drug Conjugate to Treat MET-Expressing
948 Cancers, Including Those that Are Unresponsive to MET Pathway Blockade. *Mol*
949 *Cancer Ther*. 2021;20(10):1966–1976.

950 36. Kast F, et al. Engineering an anti-HER2 biparatopic antibody with a multimodal
951 mechanism of action. *Nat Commun*. 2021;12(1):3790.

952 37. Li JY, et al. A Biparatopic HER2-Targeting Antibody-Drug Conjugate Induces Tumor
953 Regression in Primary Models Refractory to or Ineligible for HER2-Targeted Therapy.
954 *Cancer Cell*. 2019;35(6):948–949.

955 38. Zhao L, et al. Targeted protein degradation: mechanisms, strategies and
956 application. *Signal Transduct Target Ther*. 2022;7(1):113.

957 39. Ianevski A, Giri AK, Aittokallio T. SynergyFinder 3.0: an interactive analysis and
958 consensus interpretation of multi-drug synergies across multiple samples. *Nucleic Acids*
959 *Res*. 2022;50(W1):W739–W743.

40. Goyal L, et al. Polyclonal Secondary FGFR2 Mutations Drive Acquired Resistance to FGFR Inhibition in Patients with FGFR2 Fusion–Positive Cholangiocarcinoma. *Cancer Discov*. 2017;7(3):252–263.

41. Wu Q, et al. Landscape of Clinical Resistance Mechanisms to FGFR Inhibitors in FGFR2-Altered Cholangiocarcinoma. *Clin Cancer Res*. 2023;30(1):198–208.

42. Cleary JM, et al. FGFR2 Extracellular Domain In-Frame Deletions Are Therapeutically Targetable Genomic Alterations That Function as Oncogenic Drivers in Cholangiocarcinoma. *Cancer Discov*. 2021;11(10):2488–2505.

43. Shi SY, et al. A biparatopic agonistic antibody that mimics fibroblast growth factor 21 ligand activity. *J Biol Chem*. 2018;293(16):5909–5919.

44. Banik SM, et al. Lysosome-targeting chimaeras for degradation of extracellular proteins. *Nature*. 2020;584(7820):291–297.

45. Zebisch M, et al. Structural and molecular basis of ZNRF3/RNF43 transmembrane ubiquitin ligase inhibition by the Wnt agonist R-spondin. *Nat Commun*. 2013;4(1):2787.

46. Schmidt MM, Wittrup KD. A modeling analysis of the effects of molecular size and binding affinity on tumor targeting. *Mol Cancer Ther*. 2009;8(10):2861–2871.

47. Mancini M, et al. An oligoclonal antibody durably overcomes resistance of lung cancer to third-generation EGFR inhibitors. *Embo Mol Med*. 2018;10(2):294–308.

48. Nagasaka M, et al. Amivantamab (JNJ-61186372) induces clinical, biochemical, molecular, and radiographic response in a treatment-refractory NSCLC patient harboring amplified triple EGFR mutations (L858R/ T790M/G796S) in cis. *Lung Cancer*. 2022;164:52–55.

49. Pirazzoli V, et al. Afatinib plus Cetuximab Delays Resistance Compared to Single-Agent Erlotinib or Afatinib in Mouse Models of TKI-Naïve EGFR L858R-Induced Lung Adenocarcinoma. *Clin Cancer Res*. 2016;22(2):426–435.

50. Wylie AA, et al. The allosteric inhibitor ABL001 enables dual targeting of BCR–ABL1. *Nature*. 2017;543(7647):733–737.

51. Ducata DD, et al. Solution Equilibrium Titration for High-Throughput Affinity Estimation of Unpurified Antibodies and Antibody Fragments. *Slas Discov*. 2015;20(10):1256–1267.

52. Hulspas R. Titration of Fluorochrome-Conjugated Antibodies for Labeling Cell Surface Markers on Live Cells. *Curr Protoc Cytom*. 2010;54(1):6.29.1-6.29.9.

53. Hideshima T, et al. Immunomodulatory drugs activate NK cells via both Zap-70 and cereblon-dependent pathways. *Leukemia*. 2021;35(1):177–188.

54. Dobin A, et al. STAR: ultrafast universal RNA-seq aligner. *Bioinformatics*. 2012;29(1):15–21.

55. Robinson MD, McCarthy DJ, Smyth GK. edgeR: a Bioconductor package for differential expression analysis of digital gene expression data. *Bioinformatics*. 2009;26(1):139–140.

1017

Figure. 1

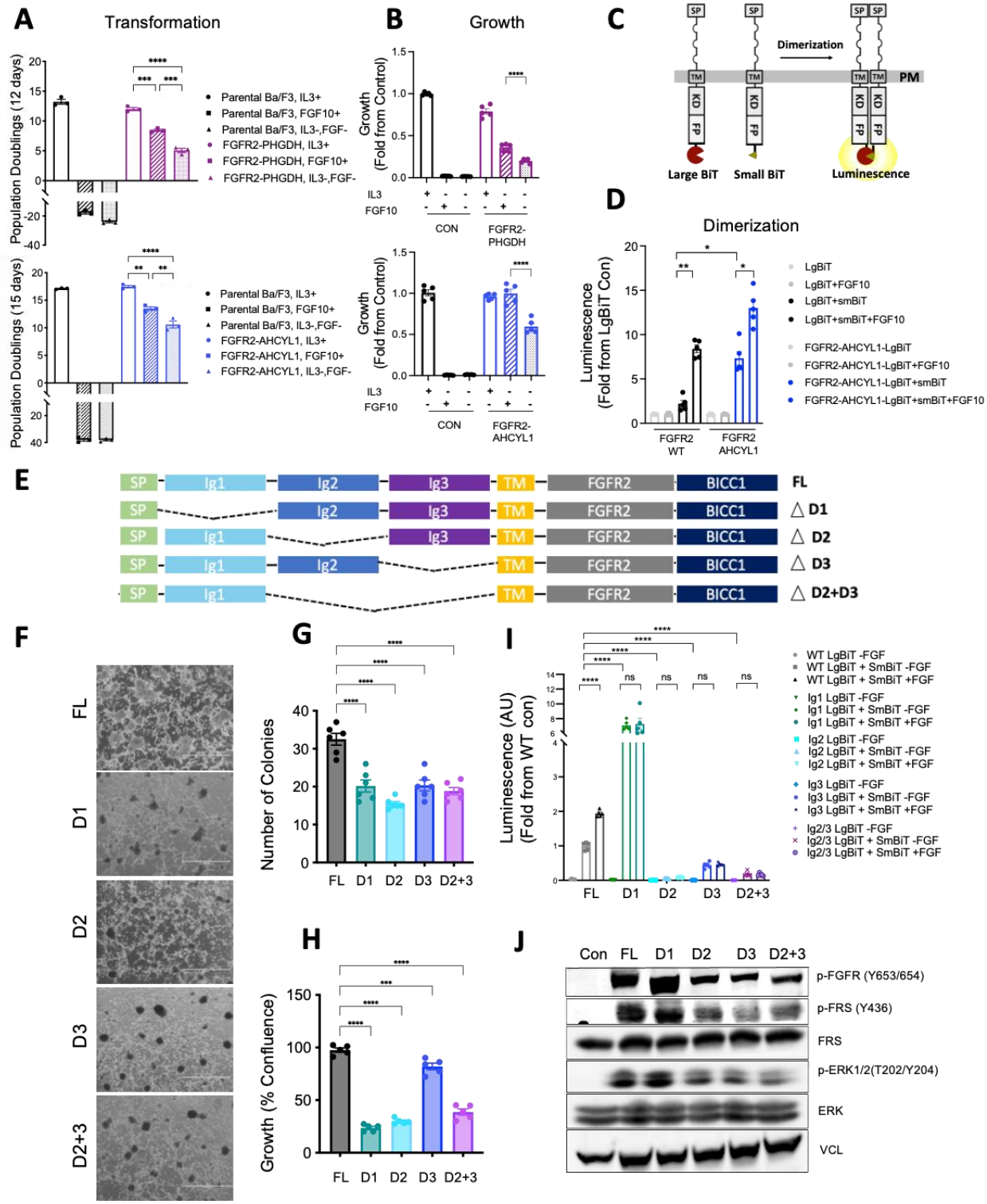

1018

Figure 1: The extracellular domain is necessary for full transformation by FGFR2 fusions.

(**A**) Transformation assays showing cumulative population doublings in BaF3 cells expressing FGFR2-PHGDH (12 days) and FGFR2-ACHYL1 (15 days) with or without FGF10 (100 ng/mL) or IL3 (10 ng/mL) as indicated (*n*=3).

(**B**) Growth of BaF3 cells expressing FGFR2-PGHDH and FGFR2-ACHYL1 analyzed by CellTiter-Glo at 5 days post IL3 removal (*n*=5).

(**C**) Illustration of the dimerization assay using FGFR2-fusion NanoBiT constructs. Large BiT and Small BiT subunits are fused to the C-terminus of FGFR2 fusions. SP: signal peptide, TM: transmembrane, KD: kinase domain, FP: fusion partner, PM: plasma membrane.

(**D**) HEK-293T cells expressing FGFR2-WT and FGFR2-ACHYL1 fused to LgBiT alone or fused to LgBiT and SmBiT were used to quantify the receptor dimerization in the presence or absence of FGF10. Shown is the fold increase over FGFR2-LgBiT activity alone (*n*=5).

(**E**) Illustration of FGFR2-BICC1 constructs with D1 (Ig1), D2 (Ig2), D3 (Ig3), or D2+D3 (Ig2+Ig3) deletions in the ECD.

(**F**) Representative images of focus formation assays of NIH-3T3 cells expressing FGFR2 WT or the indicated ECD deletion variants.

(**G**) Quantification of number of colonies from Figure 1F (*n*=6).

(**H**) Growth of NIH3T3 cells overexpressing FL, D1, D2, D3, and D2+3 deleted FGFR2-BICC1 constructs as measured by Incucyte at 5 days post plating (*n*=5).

(**I**) Dimerization of FGFR2-BICC1 D1, D2, D3, or D2+D3 ECD deleted constructs in HEK-293T cells compared to full-length FGFR2-BICC1. Fold change in luminescence over FGFR2-WT-LgBiT is shown (*n*=5).

(**J**) Immunoblotting of FGFR2 downstream pathway effectors in HEK-293 cells expressing FGFR2-BICC1 ECD deletion constructs.

All data are mean ± SEM. Data are representative of one out of three independent experiments. ns=not significant, *P < 0.05, **P < 0.01, ***P < 0.001, ****P < 0.0001 by One-way ANOVA multiple comparisons.

Figure. 2

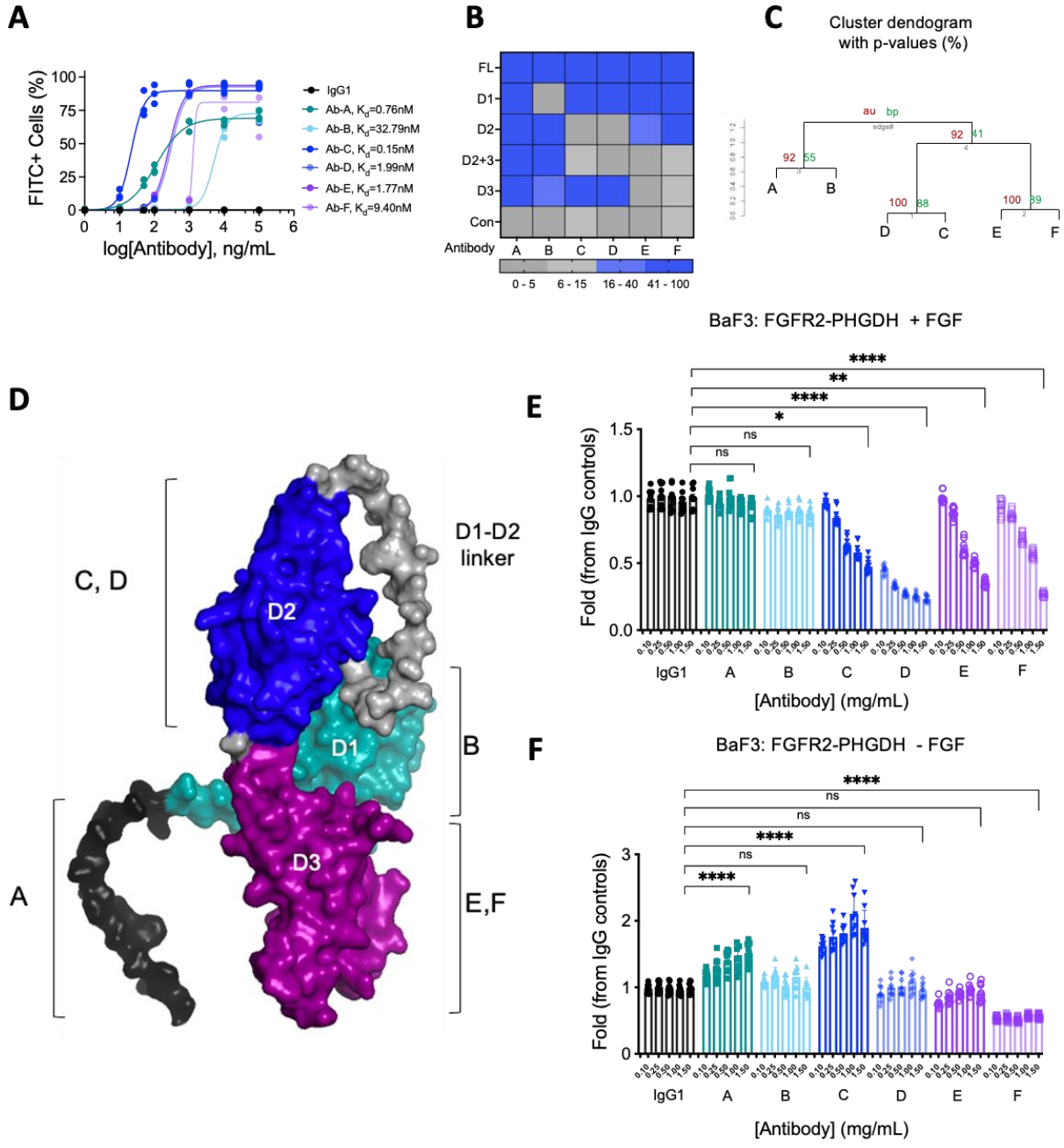
A
FITC+ Cells (%)
log[Antibody], ng/mL
IgG1
Ab-A, Kd=0.76nM
Ab-B, Kd=32.79nM
Ab-C, Kd=0.15nM
Ab-D, Kd=1.99nM
Ab-E, Kd=1.77nM
Ab-F, Kd=9.40nM
B
FL
D1
D2
D2+3
D3
Con
Antibody
0 - 5
6 - 15
16 - 40
41 - 100
C
Cluster dendogram with p-values (%)
au
bp
D
C, D
D2
D1
D3
A
B
E,F
D1-D2 linker
E
BaF3: FGFR2-PHGDH + FGF
Fold (from IgG controls)
[Antibody] (mg/mL)
F
BaF3: FGFR2-PHGDH - FGF

Figure 2: Development of candidate biparatopic antibodies directed against FGFR2

(**A**) Anti-FGFR2 antibodies (Ab-A, Ab-B, Ab-C, Ab-D, Ab-E, and Ab-F) binding to SNU16 cells (FGFR2 amplification) by flow cytometry and their associated apparent Kd values. Anti-hIgG1-FITC secondary antibody was used to detect FGFR2 parental antibodies A-F (*n*=3).

(**B**) Flow cytometry analysis using anti-hIgG1-FITC secondary antibody to detect FGFR2 parental antibodies A-F. Binding epitopes of parental antibodies A-F along the FGFR2 ECD were identified using full-length, D1, D2, D3, and D2+3 deleted FGFR2-BICC1 overexpressing NIH3T3 cell lines shown in Figure 1.

(**C**) Epitope binning through cross competition assay. BLI-Octet Epitope clustering diagrams showing cluster dendrogram with au (approximately unbiased) p-values and bp (bootstrap probability) value (%). Distance represents correlations and cluster method is average.

(**D**) Alpha-fold predicted structure of FGFR2 ECD showing D1, D2, D3 and D1-D2 flexible linker as well as 6 FGFR2 parental antibody binding epitopes A-F.

(**E-F**) Viability of FGFR2-PHGDH overexpressing BaF3 cells upon treatment with increasing concentrations of antibody A-F in the presence or absence of FGF10 ligand (*n*=9).

All data are mean ± SEM. Data are representative of one out of two independent experiments. ns=not significant, *P < 0.05, **P < 0.01, ***P < 0.001, ****P < 0.0001 by One-way ANOVA multiple comparisons.

Figure. 3

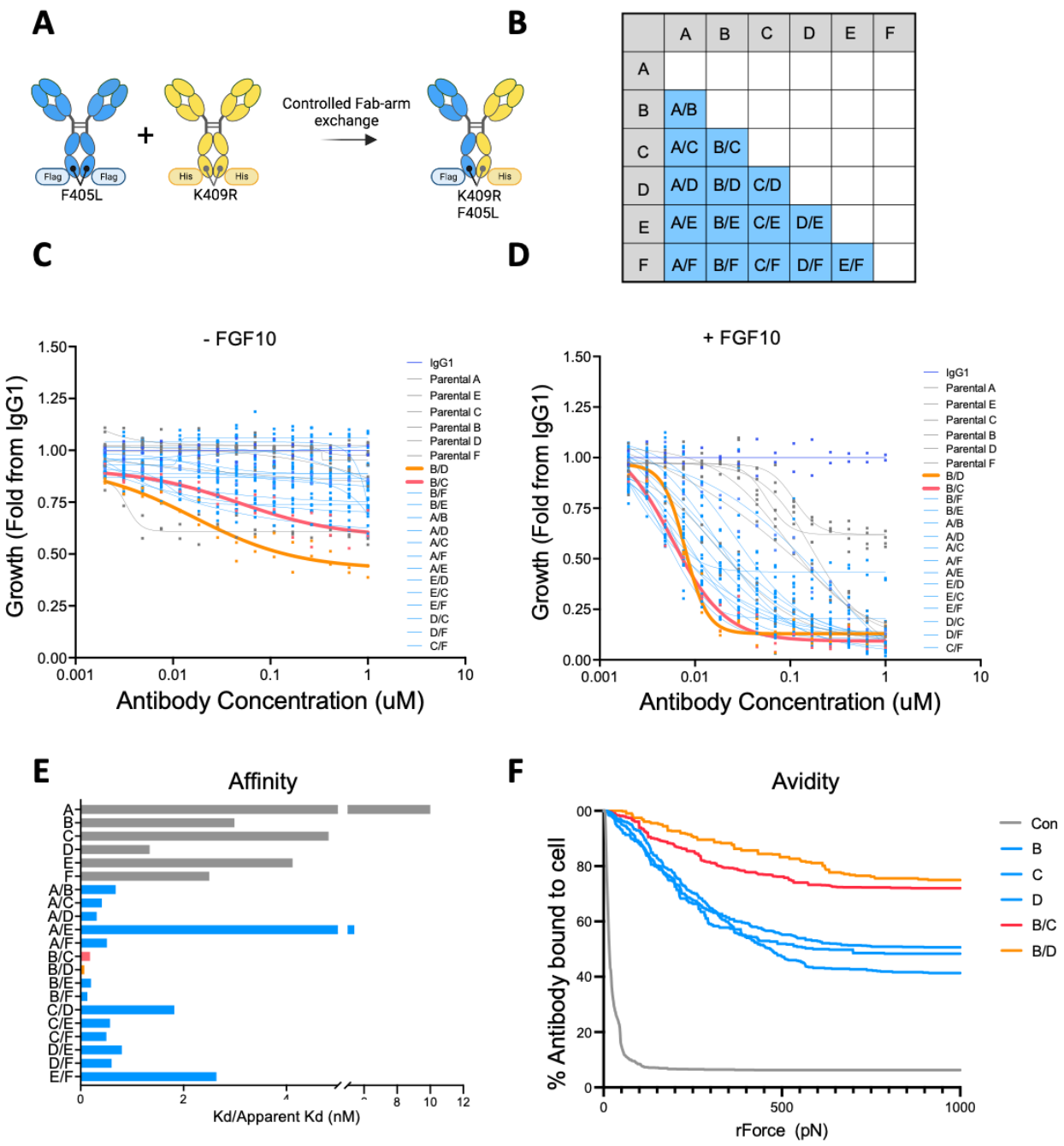

	A	B	C	D	E	F
A						
B	A/B					
C	A/C	B/C				
D	A/D	B/D	C/D			
E	A/E	B/E	C/E	D/E		
F	A/F	B/F	C/F	D/F	E/F	

1091

1092

1093

Figure 3: Identification of potent tumor growth-inhibiting biparatopic antibodies via unbiased screening

(**A**) Illustrations showing strategy for biparatopic antibody generation.

(**B**) A diagram showing all 15 possible biparatopic antibody pairs that were generated from 6 parental antibodies A-F.

(**C-D**) Viability of FGFR2-ACHYL1 overexpressing BaF3 cells upon treatment with IgG1, biparatopic antibodies, and their parental antibodies in the absence (**C**) and presence of FGF10 (**D**) (*n*=2). Data are representative of one out of two independent experiments.

(**E**) Binding affinities (Kd, nM) of parental antibodies (gray) compared to biparatopic antibodies (blue) from MSD-SET assay. Biparatopic antibodies bpAb-B/D and bpAb-B/C showed apparent binding affinities (apparent Kd) of 0.07 nM (orange bar) and 0.18 nM (pink bar) respectively (*n*=2). Data are representative of one independent experiment.

(**F**) Representative binding curves illustrating the binding avidity between FGFR2-PHGDH expressing NIH3T3 cells and antibody B, D, C or biparatopic antibody bpAb-B/C and bpAb-B/D via acoustic force spectroscopy (*n*=4-6). Data are representative of one independent experiment.

Figure. 4

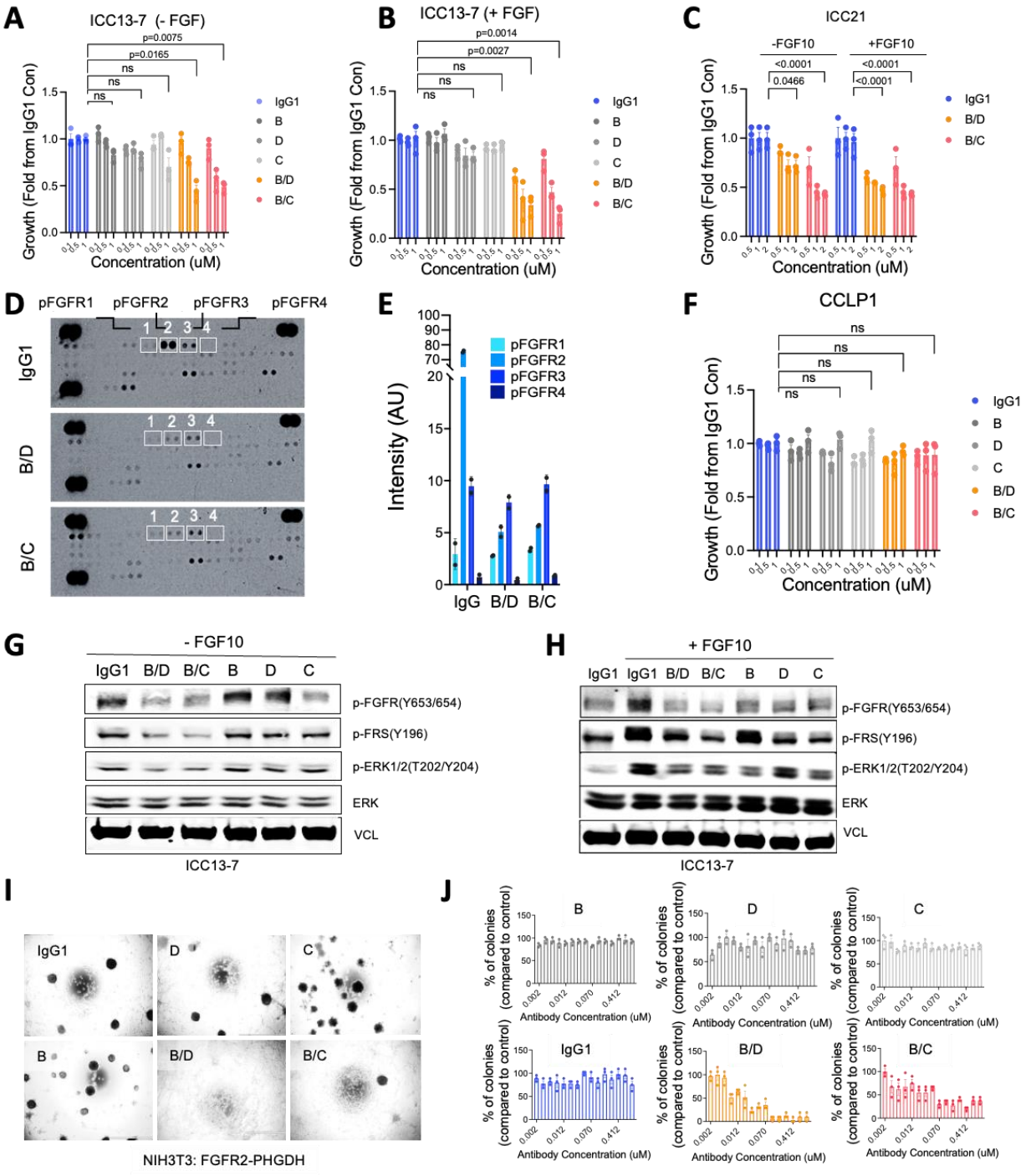
A
ICC13-7 (- FGF)
p=0.0075
p=0.0165
ns
ns
ns
Growth (Fold from IgG1 Con)
Concentration (uM)
IgG1
B
D
C
B/D
B/C
B
ICC13-7 (+ FGF)
p=0.0014
p=0.0027
ns
ns
ns
C
ICC21
-FGF10
+FGF10
<0.0001
0.0466
<0.0001
<0.0001
D
pFGFR1
pFGFR2
pFGFR3
pFGFR4
IgG1
B/D
B/C
1 2 3 4
E
Intensity (AU)
pFGFR1
pFGFR2
pFGFR3
pFGFR4
IgG
B/D
B/C
F
CCLP1
ns
ns
ns
ns
ns
G
- FGF10
IgG1 B/D B/C B D C
p-FGFR(Y653/654)
p-FRS(Y196)
p-ERK1/2(T202/Y204)
ERK
VCL
ICC13-7
H
+ FGF10
IgG1 IgG1 B/D B/C B D C
p-FGFR(Y653/654)
p-FRS(Y196)
p-ERK1/2(T202/Y204)
ERK
VCL
ICC13-7
I
IgG1
D
C
B
B/D
B/C
NIH3T3: FGFR2-PHGDH
J
B
D
C
IgG1
B/D
B/C
% of colonies (compared to control)
Antibody Concentration (uM)
0.002
0.012
0.070
0.412

Figure 4: Biparatopic antibodies show superior inhibition of growth and transformation of a FGFR2 fusion-driven cholangiocarcinoma cell line.

(**A-C**) Viability of cholangiocarcinoma cell line ICC13-7 or ICC21 upon treatment with biparatopic antibodies bpAb-B/C, bpAb-B/D, parental antibodies B, D, C or IgG1 isotype in the absence (**A, C**) or presence (**B, C**) of FGF10 at 14 days post seeding (*n*=3).

(**D-E**) Proteome profiler human phospho-kinase array demonstrating levels of 43 phosphorylated human kinases in NIH3T3 cells overexpressing FGFR2-PHGDH treated with IgG1, bpAb-B/C, or bpAb-B/D. bpAb-B/C and bpAb-B/D for 5 h (**D**). (**E**) Quantification of levels of p-FGFR1, p-FGFR2, p-FGFR3, and p-FGFR4 (white boxes) (*n*=2).

(**F**) Viability of CCLP-1 cells upon treatment with biparatopic antibodies bpAb-B/C, bpAb-B/D, parental antibodies B, D, C or IgG1 isotype control (*n*=3).

(**G-H**) Immunoblot of ICC13-7 cells upon 5 h after treatments with bpAb-B/C, or bpAb-B/D compared to the parental antibodies B, D, C in the absence (**G**) or presence (**H**) of FGF10 ligand.

(**I-J**) Representative images of focus formation assays of FGFR2-PHGDH expressing NIH3T3 cells upon treatments with parental antibodies B, D, C, biparatopic antibodies bpAb-B/C and bpAb-B/D or IgG1 (**I**) as quantified by the number of colonies (**J**) (*n*=3).

All data are mean ± SEM. Data are representative of one out of two independent experiments. ns=not significant, *P < 0.05, **P < 0.01, ***P < 0.001, ****P < 0.0001 by One-way ANOVA multiple comparisons.

Figure. 5

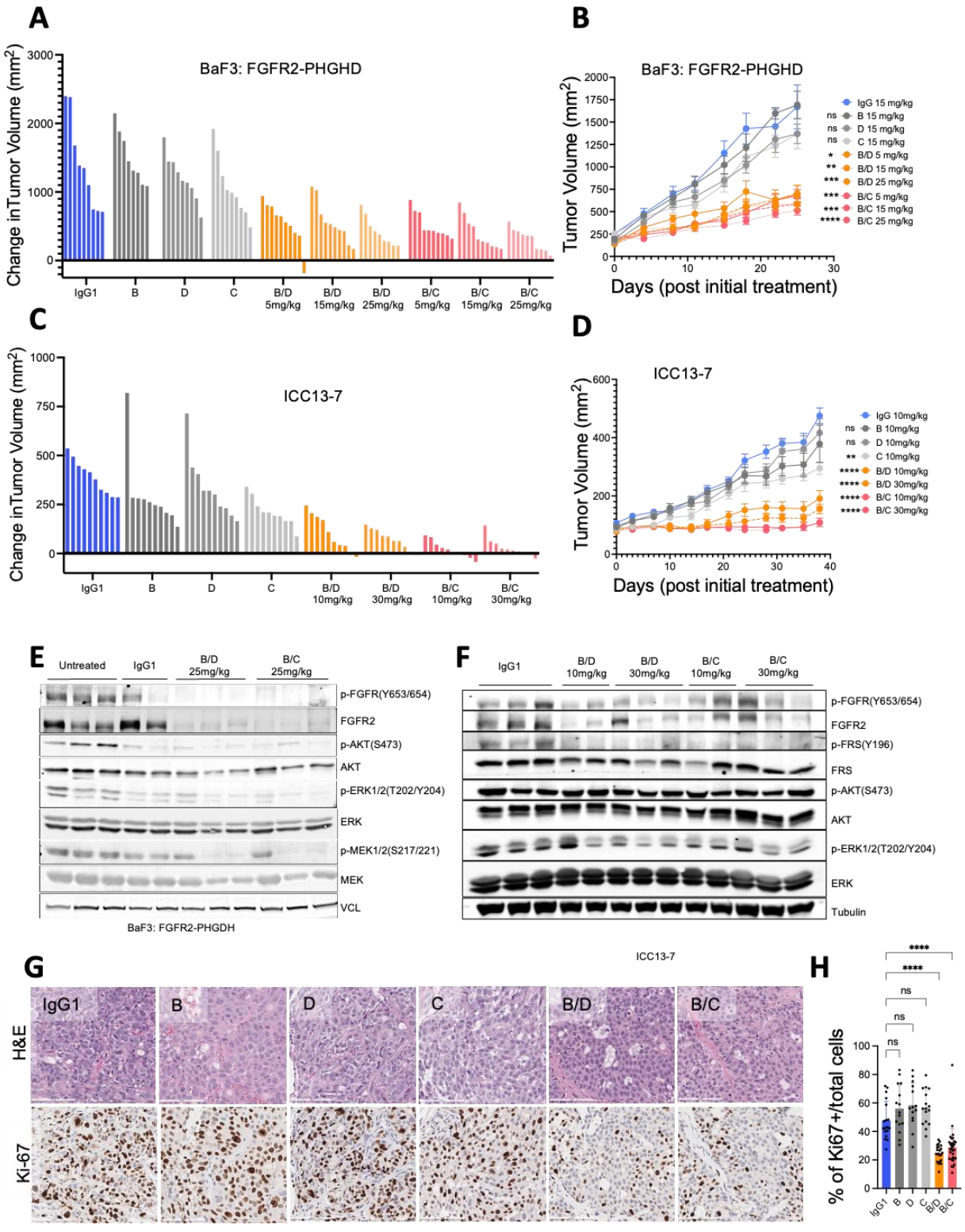
A
BaF3: FGFR2-PHGHD
Change inTumor Volume (mm2)
IgG1
B
D
C
B/D 5mg/kg
B/D 15mg/kg
B/D 25mg/kg
B/C 5mg/kg
B/C 15mg/kg
B/C 25mg/kg
B
BaF3: FGFR2-PHGHD
Tumor Volume (mm2)
Days (post initial treatment)
IgG 15 mg/kg
B 15 mg/kg
D 15 mg/kg
C 15 mg/kg
B/D 5 mg/kg
B/D 15 mg/kg
B/D 25 mg/kg
B/C 5 mg/kg
B/C 15 mg/kg
B/C 25 mg/kg
C
ICC13-7
Change inTumor Volume (mm2)
IgG1
B
D
C
B/D 10mg/kg
B/D 30mg/kg
B/C 10mg/kg
B/C 30mg/kg
D
ICC13-7
Tumor Volume (mm2)
Days (post initial treatment)
IgG 10mg/kg
B 10mg/kg
D 10mg/kg
C 10mg/kg
B/D 10mg/kg
B/D 30mg/kg
B/C 10mg/kg
B/C 30mg/kg
E
Untreated
IgG1
B/D 25mg/kg
B/C 25mg/kg
p-FGFR(Y653/654)
FGFR2
p-AKT(S473)
AKT
p-ERK1/2(T202/Y204)
ERK
p-MEK1/2(S217/221)
MEK
VCL
BaF3: FGFR2-PHGDH
F
IgG1
B/D 10mg/kg
B/D 30mg/kg
B/C 10mg/kg
B/C 30mg/kg
p-FGFR(Y653/654)
FGFR2
p-FRS(Y196)
FRS
p-AKT(S473)
AKT
p-ERK1/2(T202/Y204)
ERK
Tubulin
G
ICC13-7
H&E
Ki-67
IgG1
B
D
C
B/D
B/C
H
% of Ki67+/total cells
ns
****

Figure 5: Biparatopic antibodies show superior in vivo anti-tumor activity compared to the parental antibodies.

(**A-D**) Tumors of BALB/c scid mice (*n*=10 per group) harboring BaF3 cells overexpressing FGFR2-PHGDH (**A, B**) or ICC13-7 (**C, D**) subcutaneous xenografts treated with parental and biparatopic antibodies. Results are represented in the waterfall plot illustrating changes in tumor volume at day 25 (**A, B**) or day 38 (**C, D**) post initial treatment (**A, C**) and as geometric mean of tumor volumes ± SEM every 3-4 days from day 0-day 25 post initial treatment (**B, D**). Data are mean ± SEM across ten mice. ns=not significant, *P < 0.05, **P < 0.01, ***P < 0.001, ****P < 0.0001 by Friedman's ANOVA multiple comparisons.

(**E**) Immunoblot analysis of FGFR2-PHGDH overexpressing BaF3 cells xenograft tumors harvested 5 h after the final round of bpAb-B/C, bpAb-B/D, or IgG1 administration at 25 days post initial treatment.

(**F**) Immunoblot analysis of ICC13-7 xenograft tumors collected 5 h after the final round of antibody administration on day 38 post initial treatment.

(**G**) Representative images of hematoxylin and eosin stains (H&E) and immunohistochemistry (IHC) staining for proliferation marker Ki-67 in ICC13-7 xenograft tumor samples on the final day of treatment. Scale bars, 100um.

(**H**) Quantification of % number of Ki-67 positive nuclei normalized to the total number of nuclei (nuclei counterstain). Data are from 2 biological replicates per treatment group with at least 14 representative images for analysis per group. Data are presented in a superplot where each color represents data points from the same biological sample.

Black dots indicate the average values for each biological sample, while black lines represent the overall average for all data points.

All data are mean ± SEM. One independent experiment was performed.

Figure. 6

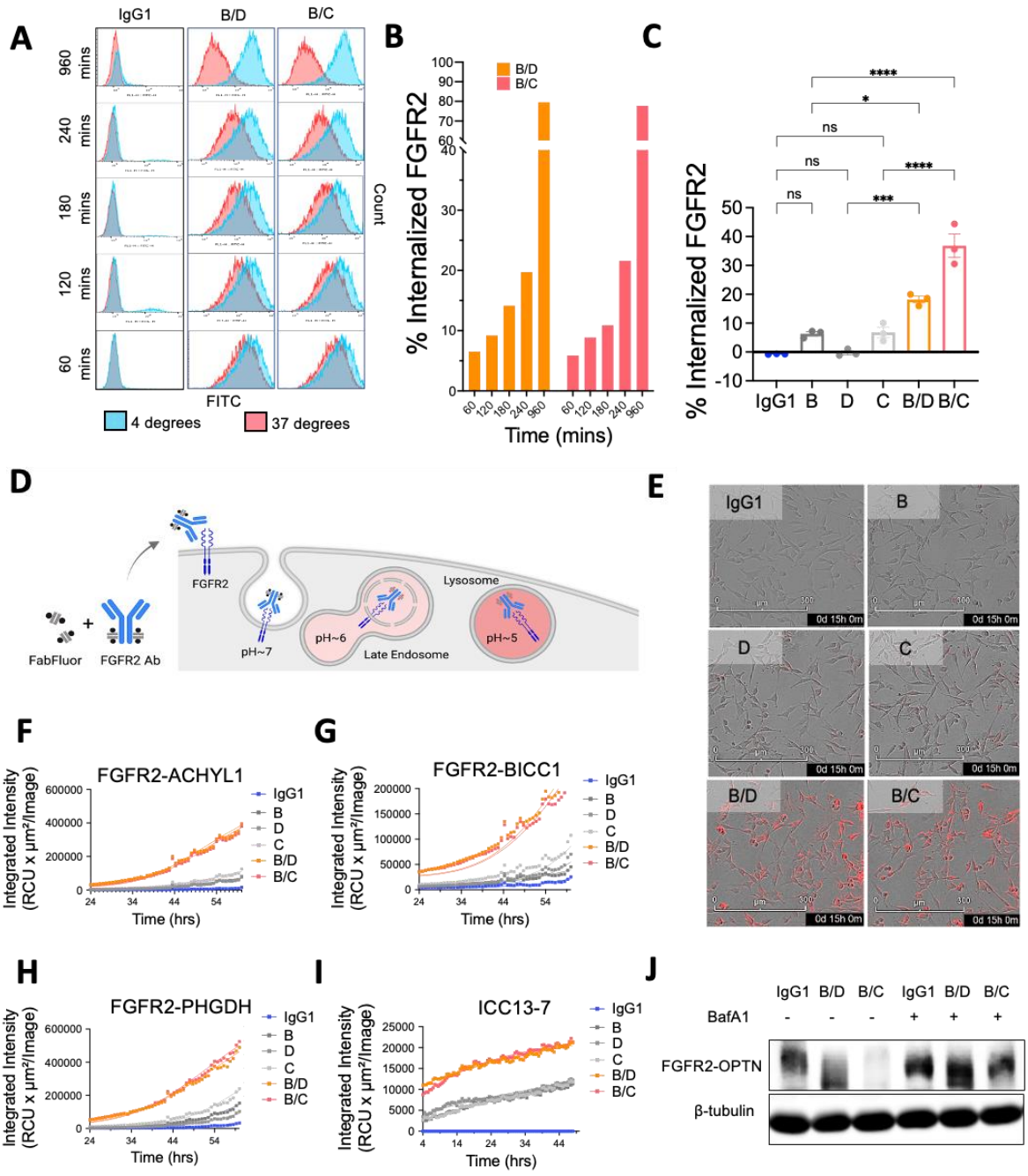

1188

1189

Figure 6: The biparatopic antibodies promote receptor internalization and lysosomal degradation.

(**A**) Flow cytometry histograms of surface FGFR2-PHGDH in BaF3 cells at 4 degrees Celsius (blue) and 37 degrees Celsius (red) upon treatment with bpAb-B/C or bpAb-B/D from 60-960 minutes.

(**B**) Quantification of the histograms demonstrating the percentage of internalized FGFR2 at 60, 120, 180, 240, and 960 minutes post bpAb-B/C or bpAb-B/D incubation.

(**C**) Quantification of histograms showing % internalized FGFR2 in ICC13-7 cell line at 4°C and 37°C after 5 h of treatment with parental antibody B, D, C or biparatopic antibodies bpAb-B/C or bpAb-B/D (*n*=3). Data are mean ± SEM. ns=not significant, *P < 0.05, **P < 0.01, ***P < 0.001, ****P < 0.0001 by One-way ANOVA multiple comparisons. Data are representative of one out of two independent experiments.

(**D**) Illustrations of Fabfluor-pH antibody labeling assay. The pH sensitive dye-based system exploits the acidic environment of the lysosomes to quantify internalization of the labeled antibody. Fluorescent signals which indicate the internalization/degradation events were tracked using Incucyte.

(**E**) Representative images of detected fluorophore in NIH3T3 cells expressing FGFR2-PHGDH treated with parental antibody B, D, C or biparatopic antibody bpAb-B/C and bpAb-B/D at 15 h post incubation.

(**F-H**) Quantification of internalization/degradation signals in FGFR2-ACHYL1 (**F**), FGFR2-BICC1 (**G**), FGFR2-PHGDH (**H**) expressing NIH3T3 cells treated with parental antibodies B, D, C or biparatopic antibody bpAb-B/C and bpAb-B/D from 24 h post incubation. Data are representative of one out of two independent experiments.

(**I**) Quantification of internalization/degradation signals in ICC13-7 cells treated with parental antibodies B, D, C or biparatopic antibody bpAb-B/C and bpAb-B/D at 4 h post incubation. Data are representative of one out of two independent experiments.
(**J**) Immunoblot of ICC13-7 cells treated with IgG1, bpAb-B/C or bpAb-B/D antibodies alone or cotreated with bafilomycin A1 (BafA1) for 24 h. BafA1 was preincubated for 1 h prior to antibody treatments. Data are representative of one independent experiment.

Figure. 7

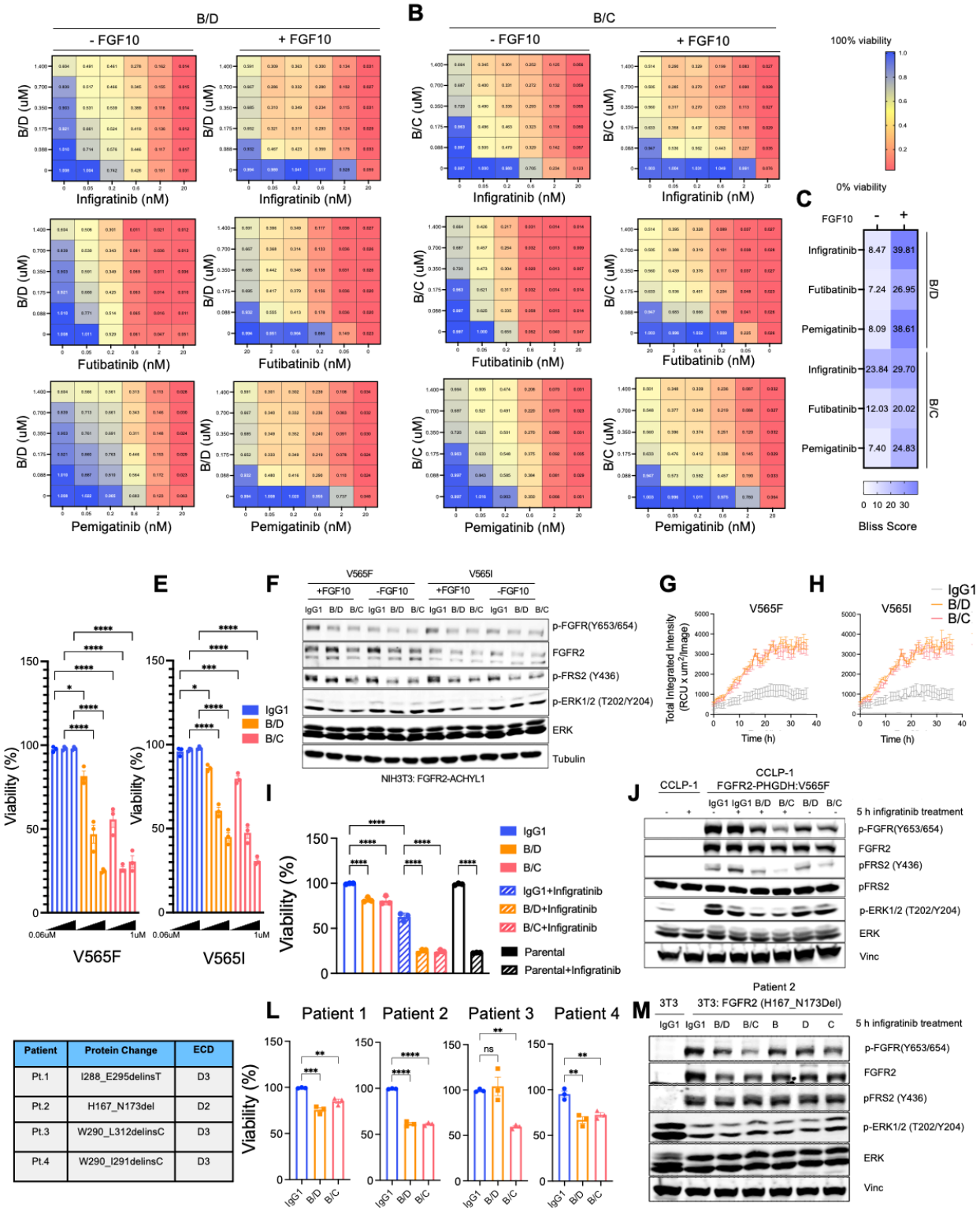

Patient	Protein Change	ECD
Pt.1	I288_E295delinsT	D3
Pt.2	H167_N173del	D2
Pt.3	W290_L312delinsC	D3
Pt.4	W290_I291delinsC	D3

Figure 7: Combinations of biparatopic antibodies with FGFR inhibitors

(**A-B**) Biparatopic antibody B/D (**A**) or B/C (**B**) with Infigratinib, Futibatinib, or Pemigatinib combination dose response matrices in the presence of absence of FGF10. 1= 100% viability and 0= 0% viability post indicated treatment.

(**C**) Heatmap showing Bliss scores calculated from dose response matrices using SynergyFinder (39) application for drug combination analysis.

(**D-E**) Viability of NIH3T3 cells stably expressed FGFR2-ACHYL1 with V565I or V565F mutations treated with bpAb-B/D, bpAb-B/C, or IgG1 (*n*=3).

(**F**) Immunoblot analysis of NIH3T3 cells stably expressed FGFR2-ACHYL1 with V565I or V565F treated with bpAb-B/D, bpAb-B/C, or IgG1 for 5 h (*n*=3).

(**G-H**) Quantification of internalization/degradation signals in FGFR2-ACHYL1 with V565I or V565F expressing NIH3T3 cells treated with biparatopic antibody bpAb-B/C, bpAb-B/D, or IgG1 from 0-38 h post incubation.

(**I**) Viability of CCLP-1 cells stably expressed FGFR2–PHGDH fusion with V565F mutation upon treatment with IgG1, bpAb-B/D or bpAb-B/C alone or in combination with Infigratinib (% compared to IgG1 treated control) (*n*=3).

(**J**) Immunoblot analysis of CCLP-1 cell line expressing FGFR2-PHGDH with V565F mutation upon treatment with IgG1, bpAb-B/C, bpAb-B/D, IgG1+Infigratinib, bpAb-B/C + Infigratinib, or bpAb-B/D + Infigratinib for 5 h.

(**K**) Deletion mutations derived from 4 different patients and the respective FGFR2 ECD.

(**L**) Viability of 4 patient derived N-terminus oncogenic mutants upon treatments with IgG1, bpAb-B/C, or bpAb-B/D as indicated (% viability compared to IgG1) (*n*=3).

(**M**) Immunoblot of NIH-3T3 cells bearing an FGFR2 H167_N173 in-frame deletion allele (patient 2) after treatment with IgG, bpAb-B/C, bpAb-B/D or the relevant parental antibodies for 5 h.

All data are mean ± SEM. Data are representative of two independent experiments. ns=not significant, *P < 0.05, **P < 0.01, ***P < 0.001, ****P < 0.0001 by One-way ANOVA multiple comparisons.